Series 01 Aerodynamics 16

Base Flow and Exhaust Plume Interaction

Part 2: Computational Study

M.M.J. Schoones/E.M. Houtman

Delft University Press

Base Flow and Exhaust Plume Interaction

Part 2: Computational Study

Series 01: Aerodynamics 16

Base Flow and Exhaust Plume Interaction

Part 2: Computational Study

M.M.J. Schoones/E.M. Houtman

Delft University Press / 1998

Published and distributed by:

Delft University Press
Mekelweg 4
2628 CD Delft
The Netherlands
Telephone +31 (0)15 278 32 54
Fax +31 (0)15 278 16 61
e-mail: DUP@DUP.TUDelft.NL

by order of:

Faculty of Aerospace Engineering
Delft University of Technology
Kluyverweg 1
P.O. Box 5058
2600 GB Delft
The Netherlands
Telephone +31 (0)15 278 14 55
Fax +31 (0)15 278 18 22
e-mail: Secretariaat@LR.TUDelft.NL
website: http://www.lr.tudelft.nl

Cover: Aerospace Design Studio, 66.5 x 45.5 cm, by:
Fer Hakkaart, Dullenbakkersteeg 3, 2312 HP Leiden, The Netherlands
Tel. +31 (0)71 512 67 25

90-407-1748-6

Printed in The Netherlands

CONTENTS

LIST OF SYMBOLS

Latin Letters

D	diameter
e	(internal) energy per unit mass
$\mathbf{e}$	unit vector in direction of solution curve
$f(s)$	distribution function
$\mathbf{f}(\mathbf{q})$	convective flux vector
$\mathbf{f}^v(\mathbf{q})$	diffusive flux vector
g_{ij}	covariant metric element in physical space
G_{ij}	covariant metric element in hyperspace
$\mathbf{g}(\mathbf{q})$	convective flux vector
$\mathbf{g}^v(\mathbf{q})$	diffusive flux vector
h	enthalpy
$\mathbf{h}(\mathbf{q})$	convective flux vector
$\mathbf{h}^v(\mathbf{q})$	diffusive flux vector
K	curvature of solution curve
L	length
M	Mach number
$N = p_{tj}/p_\infty$	ratio of jet stagnation pressure to free stream static pressure
p	pressure
$\mathbf{q}$	vector of conserved variables
Q	mesh property
r	spherical radius, radial co-ordinate
$\mathbf{r}$	position vector in physical space
Re	Reynolds number
R	radius
$\mathbf{R}$	position vector in hyperspace
s	arc length
T	temperature
$\mathbf{T}$	rotation matrix
u(x), u(s)	solution curve
u	Cartesian velocity component in x direction
v	Cartesian velocity component in y direction
w	Cartesian velocity component in z direction
w(x), w(s)	weight function
x	axial distance measured from base
y	lateral distance, y=0 at model vertical symmetry plane
z	co-ordinate pointing upwards, z=0 at model horizontal symmetry plane

Greek Letters

α	flow expansion angle, constant
β	constant
κ	thermal conductivity coefficient
χ	co-ordinate transformed from axial co-ordinate x
δ_N	nozzle half angle
γ	ratio of specific heat
θ	polar co-ordinate and streamline angle
ρ	density
τ	shear stress
μ	viscosity coefficient
ν	Prandtl-Meyer angle
φ	angle between barrel shock and upstream streamline
$\xi(s)$	smooth, continuously increasing mathematical function
ξ	co-ordinate transformed from radial co-ordinate r
ϕ	azimuthal angle at base, $\phi = 0$ at top of model

Subscripts

b	jet boundary, base
c	curvature
e	nozzle exit
E	after expansion
j	jet
p	Pitot
pl	jet plume
t	total, stagnation
∞	infinity

Chapter 1

INTRODUCTION

A combined experimental and computational study of the flow field along an axi-symmetric body with a single operating exhaust nozzle has been made for the FESTIP Aerothermodynamics [4] investigation. This study was carried out in the scope of the Future European Space Transportation Investigations Program (FESTIP) in the Delft University of Technology transonic/supersonic wind tunnel and was part of a joint computational/experimental research program on base flow-jet plume interactions. The model was mounted in supersonic free streams of Mach 1.96 and 2.98, the jet exhausting from the nozzle had an exit Mach number of 4 and operated at various jet stagnation pressures. The Reynolds numbers based on the length of the model were greater than $5 \cdot 10^6$. In addition, to ascertain a turbulent boundary layer, the boundary layer on the model was tripped for accurate comparison with numerical simulations. The present investigation embroiders on this theme.

The supersonic jet emanating from the centrally protruding exhaust nozzle in the base interacts with the external main flow around the body. In the interaction zone a turbulent mixing layer, a re-circulation region and a shock system, consisting of a plume shock and a barrel shock, are formed. Flow reattachment at the base, important with respect to heat-transfer, is likely. The present report aims to investigate these different flow phenomena.

Various numerical simulations will be considered, in order to obtain an accurate physical representation of the interaction zone. Euler and Navier-Stokes numerical simulations will be put to use in combination with regular meshes. It is questioned whether or not specific simulation techniques might provide a better physical representation of the flow field. In this respect, special attention has to be paid to mesh generation. Mesh generation has to provide an adequate resolution of the geometry of the flow domain and has to capture the flow features. In order to satisfy the latter requirement it is necessary to couple the mesh generating process with the flow algorithm. In the current investigation adaptation of the mesh to capture the flow features has been composed and used in combination with Navier-Stokes simulation techniques.

Chapter 2

DESCRIPTION OF UNDER-EXPANDED JETS

The structure of under-expanded jets has, among others, been investigated in detail by Adamson & Nicholls [1], Moran [9], and Peters & Phares [12]. These three studies are restricted to plumes exhausting into quiescent media. In the present (two-dimensional) description the results of these studies are extrapolated to under-expanded jets in a co-flowing supersonic free stream. A more detailed description of the structure of under-expanded jets in a co-flowing supersonic flow can be found in [14].

The pressure at the exit of an isentropic supersonic nozzle is a function of the upstream stagnation pressure and the nozzle to throat area ratio. The ambient pressure and the static pressure at the nozzle exit will generally show a difference in magnitude. The jet is called under-expanded when the exit pressure of the exhaust gas, p_e, is higher than the ambient pressure. The following description is based on the under-expanded jet.

When the nozzle operates at design conditions, i.e., the Mach number M_e at the nozzle exit has reached its design value, the exhaust air expands in a fan centred at the nozzle lip (Fig. 2.1). Streamlines close to the nozzle wall are deflected through an angle α, sufficient to expand the gas to the ambient pressure. More inside the jet the flow is expanded more and causes the gas to fall to pressures below the ambient pressure. Recompression to the ambient pressure partly takes place through compression waves, formed at the intersection of expansion waves with the jet boundary, coalescing into the barrel shock. The barrel shock is a line of demarcation between the interior region, which is independent of the ambient pressure, and the outer region, which is influenced by the ambient pressure.

The jet flow upstream of the barrel shock assumes a source-like nature, and can be described by the source-flow-model. The barrel shock is an oblique axi-symmetric shock that is being driven towards the nozzle axis by the external pressure further downstream. Through the expansion at the nozzle lip the exhaust gas acquires a velocity of which the radial component initially sweeps the barrel shock away from the nozzle axis. The flow downstream of the barrel shock is rotational as the barrel shock strengthens with distance from the nozzle exit (compression waves coalesce into the barrel shock) producing an entropy gradient across the shock layer. The 'inner shock layer' covers the region between the jet boundary and the barrel shock and contains the jet boundary and the shear layer growing along the jet boundary. To allow the gas to follow the curvature of the barrel shock a significant static pressure gradient across the shock layer due to the centrifugal acceleration is also required. The under-expanded jet in a co-flowing supersonic

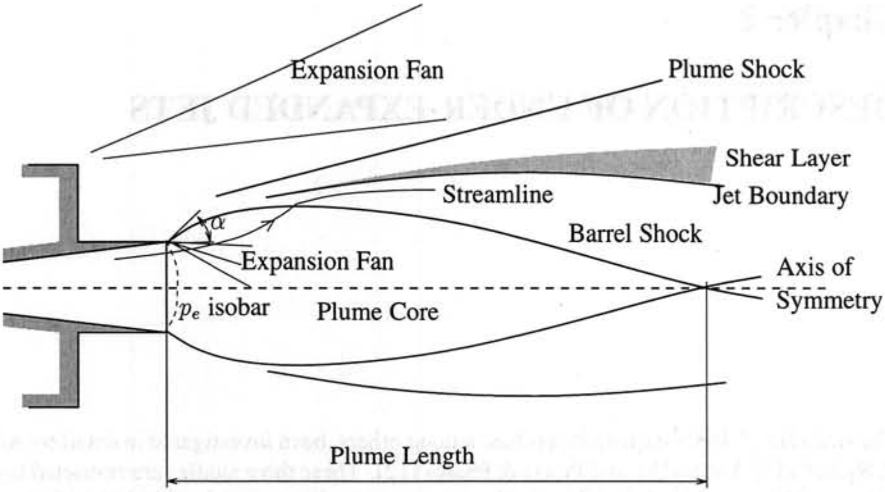

Figure 2.1: Schematic Geometry of an Under-expanded Jet

stream has got, in contrary to an under-expanded jet issuing into a quiescent gas, a boundary of inconstant pressure.

The external flow, which has been deflected by the centered expansion at the end of the model, again changes direction because of the expanding jet and an oblique shock, called the plume shock, develops in the supersonic external stream. Consequently the pressure at the jet boundary is increased. Compared to its quiescent counterpart the expansion of the plume is significantly reduced this way. When the plume jet boundary turns back towards the nozzle axis, the free stream expands and as a result the ambient pressure drops. This in turn tends to reduce the contraction of the jet. Both processes help to adjust the jet pressure to the ambient pressure and tend to dampen the formation of downstream shock cells, which are evidently present in the flow field of under-expanded jets issuing into quiescent media. The mechanism of adjusting the jet pressure to the ambient pressure is called the 'supersonic pressure relief effect'.

In the case of moderately and highly under-expanded jets the barrel shock is too strong to reflect in a regular manner from the axis of symmetry. A Mach stem is formed which in the axi-symmetric case is known as a Mach disc. Cain [5] clearly describes this phenomenon. Peters & Phares [12] showed that in the case of slightly under-expanded jets, like in the cases studied in the present investigation, the barrel shock reflects in a regular manner from the axis of symmetry.

Chapter 3

NUMERICAL METHOD

3.1 Governing Equations

In a Cartesian co-ordinate system the Navier-Stokes equations, expressing conservation of mass, momentum and energy for a compressible perfect gas, formulated in conservative form are

$$\frac{\partial \mathbf{q}}{\partial t} + \frac{\partial \mathbf{f}(\mathbf{q})}{\partial x} + \frac{\partial \mathbf{g}(\mathbf{q})}{\partial y} + \frac{\partial \mathbf{h}(\mathbf{q})}{\partial z} - \frac{\partial \mathbf{f}^v(\mathbf{q})}{\partial x} - \frac{\partial \mathbf{g}^v(\mathbf{q})}{\partial y} - \frac{\partial \mathbf{h}^v(\mathbf{q})}{\partial z} = 0 \tag{3.1}$$

where $\mathbf{q}$ is the vector of the conserved variables

$$\mathbf{q} = (\rho, \rho u, \rho v, \rho w, \rho\, e_t)^T, \tag{3.2}$$

$\mathbf{f}(\mathbf{q})$, $\mathbf{g}(\mathbf{q})$ and $\mathbf{h}(\mathbf{q})$ are the convective flux vectors

$$\begin{aligned}
\mathbf{f}(\mathbf{q}) &= \left(\rho u\,, \rho u^2 + p\,, \rho uv\,, \rho uw\,, \rho u h_t\right)^T \\
\mathbf{g}(\mathbf{q}) &= \left(\rho v\,, \rho uv\,, \rho v^2 + p\,, \rho vw\,, \rho v h_t\right)^T \\
\mathbf{h}(\mathbf{q}) &= \left(\rho w\,, \rho uw\,, \rho vw\,, \rho w^2 + p\,, \rho w h_t\right)^T
\end{aligned} \tag{3.3}$$

and $\mathbf{f}^v(\mathbf{q})$, $\mathbf{g}^v(\mathbf{q})$ and $\mathbf{h}^v(\mathbf{q})$ are the diffusive flux vectors, which are for a Newtonian fluid with the Stokes relation for the viscosity coefficients given by

$$\begin{aligned}
\mathbf{f}^v(\mathbf{q}) &= \left(0, \mu\tau_{xx}\,, \mu\tau_{xy}\,, \mu\tau_{xz}\,, u\mu\tau_{xx} + v\mu\tau_{xy} + w\mu\tau_{xz} + k\frac{\partial T}{\partial x}\right)^T \\
\mathbf{g}^v(\mathbf{q}) &= \left(0, \mu\tau_{yx}\,, \mu\tau_{yy}\,, \mu\tau_{yz}\,, u\mu\tau_{yx} + v\mu\tau_{yy} + w\mu\tau_{yz} + k\frac{\partial T}{\partial y}\right)^T \\
\mathbf{h}^v(\mathbf{q}) &= \left(0, \mu\tau_{zx}\,, \mu\tau_{zy}\,, \mu\tau_{zz}\,, u\mu\tau_{zx} + v\mu\tau_{zy} + w\mu\tau_{zz} + k\frac{\partial T}{\partial z}\right)^T
\end{aligned} \tag{3.4}$$

Here ρ is the density; u, v, w are the Cartesian velocity components in the x, y, z directions respectively; p is the static pressure; T is the static temperature; μ is the viscosity coefficient; k the thermal conductivity coefficient; e_t is the total energy per unit of mass given by e_t =

$e+\frac{1}{2}(u^2+v^2+w^2)$, in which e is the internal energy per unit of mass; h_t is the total enthalpy given by $h_t = e_t + p/\rho$. For a calorically perfect gas the equation of state may be expressed as:

$$p = (\gamma - 1)\rho e = (\gamma - 1)\rho \left(e_t - \frac{1}{2}\left(u^2 + v^2 + w^2\right)\right)$$

in which the ratio of specific heats $\gamma = c_p/c_v$ may be considered as constant ($\gamma = 1.4$). The shear stresses in the diffusive flux vectors are given by:

$$\begin{aligned}
\tau_{xx} &= +\frac{4}{3}\frac{\partial u}{\partial x} - \frac{2}{3}\frac{\partial v}{\partial y} - \frac{2}{3}\frac{\partial w}{\partial z} \\
\tau_{yy} &= -\frac{2}{3}\frac{\partial u}{\partial x} + \frac{4}{3}\frac{\partial v}{\partial y} - \frac{2}{3}\frac{\partial w}{\partial z} \\
\tau_{zz} &= -\frac{2}{3}\frac{\partial u}{\partial x} - \frac{2}{3}\frac{\partial v}{\partial y} + \frac{4}{3}\frac{\partial w}{\partial z} \\
\tau_{xy} = \tau_{yx} &= \frac{\partial v}{\partial x} + \frac{\partial u}{\partial y} \\
\tau_{xz} = \tau_{zx} &= \frac{\partial u}{\partial z} + \frac{\partial w}{\partial x} \\
\tau_{yz} = \tau_{zy} &= \frac{\partial w}{\partial y} + \frac{\partial v}{\partial z}
\end{aligned} \tag{3.5}$$

In order to obtain a convenient non-dimensional form of the Navier-Stokes equations, the coordinates are scaled with a characteristic length L_{ref}, the velocity components by a characteristic speed U_{ref}, the density by some characteristic density ρ_{ref}, and consequently, the time by L_{ref}/U_{ref}, the pressure by $\rho_{ref}U_{ref}^2$ and the temperature by U_{ref}^2/c_v. If we maintain the same notation for the non-dimensional variables, the convective flux vectors Eq. (3.3) do not change, while the diffusive flux vectors Eq. (3.4) become:

$$\begin{aligned}
\mathbf{f}^v(\mathbf{q}) &= \frac{1}{Re}\left(0, \tau_{xx}, \tau_{xy}, \tau_{xz}, u\tau_{xx} + v\tau_{xy} + w\tau_{xz} + \frac{\gamma}{Pr}\frac{\partial T}{\partial x}\right)^T \\
\mathbf{g}^v(\mathbf{q}) &= \frac{1}{Re}\left(0, \tau_{yx}, \tau_{yy}, \tau_{yz}, u\tau_{yx} + v\tau_{yy} + w\tau_{yz} + \frac{\gamma}{Pr}\frac{\partial T}{\partial y}\right)^T \\
\mathbf{h}^v(\mathbf{q}) &= \frac{1}{Re}\left(0, \tau_{zx}, \tau_{zy}, \tau_{zz}, u\tau_{zx} + v\tau_{zy} + w\tau_{zz} + \frac{\gamma}{Pr}\frac{\partial T}{\partial z}\right)^T
\end{aligned} \tag{3.6}$$

in which $Re = \rho_{ref}U_{ref}L_{ref}/\mu$ is a Reynolds number, $Pr = \mu c_p/k$ the Prandtl number which may be considered constant ($Pr = 0.72$). The viscosity coefficient μ is calculated according to Sutherland's law:

$$\frac{\mu}{\mu_{ref}} = \left(\frac{T}{T_{ref}}\right)^{3/2}\frac{T_{ref} + S_{suth}}{T + S_{suth}} \tag{3.7}$$

in which $S_{suth} = 110.4$K is taken constant, $T_{ref} = 288.15$K and $\mu_{ref} = 1.7894 \times 10^{-5}$kg/m s. The Reynolds number measures the ratio between convection and diffusion. Most flow which are of aerodynamic interest have $Re \gg 1$, and hence are convection dominated. In the diffusive operator, the Prandtl number is the ratio of viscous and heat conduction terms. For air $Pr = O(1)$, which has the consequence that the diffusion of kinetic and thermal energy is of the same order of magnitude. This implies approximately equally thick kinetic and thermal boundary layers.

3.2 Finite Volume Discretization

The discretization method for the Navier-Stokes equations Eq. (3.1) uses the integral form of the equations in order to allow Euler solutions with discontinuities for $1/Re \to 0$. A straightforward and simple discretization of the Navier-Stokes equations in integral form is obtained by subdividing the computational domain V into disjunct hexahedral finite volumes V_{ijk} ($i = 1, 2, \dots, N_i$, $j = 1, 2, \dots, N_j$ and $k = 1, 2, \dots, N_k$) and by requiring the conservation laws for each finite volume separately:

$$\iiint\limits_{V_{ijk}} \frac{\partial \mathbf{q}_{ijk}}{dt} + \iint\limits_{S_{ijk}} (\mathbf{f}(\mathbf{q})n_x + \mathbf{g}(\mathbf{q})n_y + \mathbf{h}(\mathbf{q})n_z)\, \mathrm{d}S$$

$$- \iint\limits_{S_{ijk}} \frac{1}{Re} (\mathbf{f}^v(\mathbf{q})n_x + \mathbf{g}^v(\mathbf{q})n_y + \mathbf{h}^v(\mathbf{q})n_z)\, \mathrm{d}S = 0 \quad (3.8)$$

where $\mathbf{n} = (n_x\,, n_y\,, n_z)^T$ is the outward unit normal vector on the boundary S_{ijk} of the volumes $\triangle V_{ijk}$, the convective fluxes $\mathbf{f}$, $\mathbf{g}$ and $\mathbf{h}$ are given by Eq. (3.3) and the diffusive $\mathbf{f}^v$, $\mathbf{g}^v$ and $\mathbf{h}^v$ are given by Eq. (3.6). The finite volume discretization requires an evaluation of the convective and diffusive fluxes at each cell face. The evaluation of the convective fluxes is done according to the Godunov principle. For this purpose upwind schemes based on approximate Riemann solutions are used. The diffusive fluxes will be evaluated with a so-called "sub-block" method.

3.3 Evaluation of the Convective Fluxes

The discretization of the convective part uses the invariance property of the Euler equations under rotation of the co-ordinate system. Thus we can write:

$$\mathbf{f}(\mathbf{q}) \cdot n_x + \mathbf{g}(\mathbf{q}) \cdot n_y + \mathbf{h}(\mathbf{q}) \cdot n_z = \mathbf{T}^{-1}\, \mathbf{f}(\mathbf{T}\, \mathbf{q}) \quad (3.9)$$

where $\mathbf{T}$ is the rotation matrix, which transforms the momentum components of the state vector $\mathbf{q}$ to a new Cartesian $\tilde{x}$, $\tilde{y}$, $\tilde{z}$ co-ordinate system in which the $\tilde{x}$-axis is aligned with the unit normal on the control volume boundary. This new Cartesian co-ordinate system has the base

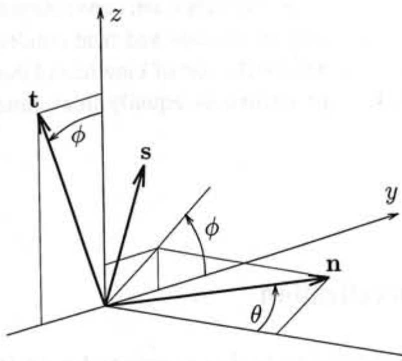

Figure 3.1: Definition of Rotated Co-ordinate Axes

vectors **n**, **s** and **t** in $\tilde{x}$, $\tilde{y}$ and $\tilde{z}$ -direction respectively (Fig. 3.1), which are:

$$\begin{aligned} \mathbf{n} &= (n_x\,, n_y\,, n_z)^T &&= (\cos\theta, \sin\theta\cos\phi, \sin\theta\sin\phi)^T \\ \mathbf{s} &= (s_x\,, s_y\,, s_z)^T &&= (-\sin\theta, \cos\theta\cos\phi, \cos\theta\sin\phi)^T \\ \mathbf{t} &= (t_x\,, t_y\,, t_z)^T &&= (0, -\sin\phi, \cos\phi)^T \end{aligned} \tag{3.10}$$

The rotation matrix **T** is defined as:

$$\mathbf{T} = \begin{pmatrix} 1 & 0 & 0 & 0 & 0 \\ 0 & n_x & n_y & n_z & 0 \\ 0 & s_x & s_y & s_z & 0 \\ 0 & t_x & t_y & t_z & 0 \\ 0 & 0 & 0 & 0 & 1 \end{pmatrix} = \begin{pmatrix} 1 & 0 & 0 & 0 & 0 \\ 0 & \cos\theta & \sin\theta\cos\phi & \sin\theta\sin\phi & 0 \\ 0 & -\sin\theta & \cos\theta\cos\phi & \cos\theta\sin\phi & 0 \\ 0 & 0 & -\sin\phi & \cos\phi & 0 \\ 0 & 0 & 0 & 0 & 1 \end{pmatrix} \tag{3.11}$$

With reference to Fig. 3.2 and with each unit normal in positive i, j or k direction, the discretization of the convective part of Eq. (3.8) may be written as:

$$\begin{aligned} \mathcal{F}_{ijk} = {} & \mathbf{T}^{-1}_{i+\frac{1}{2}\,jk}\,\mathbf{f}\left(\mathbf{T}_{i+\frac{1}{2}\,jk}\,\mathbf{q}_{i+\frac{1}{2}\,jk}\right)\Delta S_{i+\frac{1}{2}\,jk} - \mathbf{T}^{-1}_{i-\frac{1}{2}\,jk}\,\mathbf{f}\left(\mathbf{T}_{i-\frac{1}{2}\,jk}\,\mathbf{q}_{i-\frac{1}{2}\,jk}\right)\Delta S_{i-\frac{1}{2}\,jk} \\ & + \mathbf{T}^{-1}_{ij+\frac{1}{2}\,k}\,\mathbf{f}\left(\mathbf{T}_{ij+\frac{1}{2}\,k}\,\mathbf{q}_{ij+\frac{1}{2}\,k}\right)\Delta S_{ij+\frac{1}{2}\,k} - \mathbf{T}^{-1}_{ij-\frac{1}{2}\,k}\,\mathbf{f}\left(\mathbf{T}_{ij-\frac{1}{2}\,k}\,\mathbf{q}_{ij-\frac{1}{2}\,k}\right)\Delta S_{ij-\frac{1}{2}\,k} \\ & + \mathbf{T}^{-1}_{ijk+\frac{1}{2}}\,\mathbf{f}\left(\mathbf{T}_{ijk+\frac{1}{2}}\,\mathbf{q}_{ijk+\frac{1}{2}}\right)\Delta S_{ijk+\frac{1}{2}} - \mathbf{T}^{-1}_{ijk-\frac{1}{2}}\,\mathbf{f}\left(\mathbf{T}_{ijk-\frac{1}{2}}\,\mathbf{q}_{ijk-\frac{1}{2}}\right)\Delta S_{ijk-\frac{1}{2}} \end{aligned} \tag{3.12}$$

in which $\mathbf{f}\left(\mathbf{T}_{i+\frac{1}{2}\,jk}\,\mathbf{q}_{i+\frac{1}{2}\,jk}\right)$ is a mean flux at the cell face $S_{i+\frac{1}{2}\,jk}$ etc. The flux vectors at the different cell faces have to be calculated by some numerical flux function. For the calculation of the numerical flux some functions belonging to the family of upwind schemes are used. Three different types of schemes have been implemented in the code: the flux-vector-splitting scheme of van Leer [8] and flux-difference-splitting schemes of Osher [11] and Roe [13]. The computations presented in this report have been obtained with the van Leer scheme. In this scheme the numerical flux function for the interface $S_{i+\frac{1}{2}\,jk}$ may be written in the form:

$$\mathbf{T}^{-1}_{i+\frac{1}{2}\,jk}\,\mathbf{f}\left(\mathbf{T}_{i+\frac{1}{2}\,jk}\,\mathbf{q}_{i+\frac{1}{2}\,jk}\right) = \mathbf{T}^{-1}_{i+\frac{1}{2}\,jk}\,\mathbf{f}_{NF}\left(\mathbf{T}_{i+\frac{1}{2}\,jk}\,\mathbf{q}^{L}_{i+\frac{1}{2}\,jk}\,, \mathbf{T}_{i+\frac{1}{2}\,jk}\,\mathbf{q}^{R}_{i+\frac{1}{2}\,jk}\right) \tag{3.13}$$

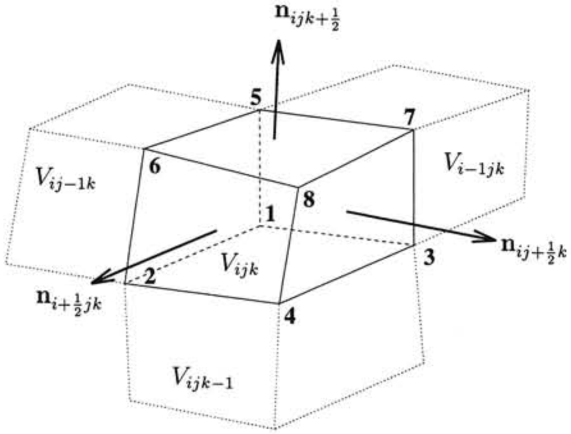

Figure 3.2: Dcfinition of Finite Volume

where $\mathbf{q}^L_{i+\frac{1}{2}jk}$ and $\mathbf{q}^R_{i+\frac{1}{2}jk}$ are the states at either side of the cell interface, obtained from an interpolation between some states $\mathbf{q}_{ijk}$ in the centres of the finite volumes. For example, in a spatially first order accurate system, the states are assumed to be constant within each volume, so we get $\mathbf{q}^L_{i+\frac{1}{2}jk} = \mathbf{q}_{ijk}$ and $\mathbf{q}^R_{i+\frac{1}{2}jk} = \mathbf{q}_{i+1jk}$.

First order accuracy, however, is too low for practical applications and discontinuities not aligned with the grid are smeared out disastrously. As has been noted by van Leer [7] the order of accuracy can be improved by using a more accurate interpolation to calculate the different components q of the state vectors $\mathbf{q}$ at both sides of a cell face, which can be written in a general form as:

$$\begin{aligned} q^L_{i+\frac{1}{2}jk} &= q_{ijk} + \tfrac{1}{4}\{(1+\kappa)\Delta_i + (1-\kappa)\nabla_i\} \\ q^R_{i-\frac{1}{2}jk} &= q_{ijk} - \tfrac{1}{4}\{(1-\kappa)\Delta_i + (1+\kappa)\nabla_i\} \end{aligned} \tag{3.14}$$

where $\Delta_i = q_{i+1jk} - q_{ijk}$ and $\nabla_i = q_{ijk} - q_{i-1jk}$ and $\kappa \in (-1,1)$. Similar formulae yield in the other co-ordinate directions. In order to avoid spurious non-monotonicity (wiggles or over- and undershoots), the interpolation has to be limited, which has the properties of second order accuracy in the smooth part of the flow field and steepening of discontinuities without introducing non-monotonicity. For the present calculations the van Albada limiter [2] is used. The van Albada limiter interpolation functions are:

$$\begin{aligned} q^L_{i+\frac{1}{2}jk} &= q_{ijk} + \frac{r^i_{ijk}}{4}\left\{(1+\kappa\, r^i_{ijk})\,\Delta_i + (1-\kappa\, r^i_{ijk})\,\nabla_i\right\} \\ q^R_{i-\frac{1}{2}jk} &= q_{ijk} - \frac{r^i_{ijk}}{4}\left\{(1-\kappa\, r^i_{ijk})\,\Delta_i + (1+\kappa\, r^i_{ijk})\,\nabla_i\right\} \end{aligned} \tag{3.15}$$

in which κ is a constant and the limiter function r^i_{ijk} in i-direction is defined as:

$$r^i_{ijk} = \frac{2\,\Delta_i\,\nabla_i\, + 2\epsilon^2}{{\Delta_i}^2 + {\nabla_i}^2 + 2\epsilon^2} \tag{3.16}$$

The constant ϵ is a small number ($\epsilon \approx 10^{-7}$), which is made proportional to the grid size ($\epsilon \sim (\text{Constant}\Delta\, x)^{3/2}$), where Δx is a characteristic mesh width [18]. This constant has a twofold objective: first to avoid dividing by zero, and second to switch off the limiting in near-constant regions of the flow. In regions of near-constant flow where ϵ^2 is dominant over $(\Delta_i)^2$ and $(\nabla_i)^2$ the unlimited $\kappa = 0$ scheme is recovered. The computations in this report with the van Albada limiter are performed with $\kappa = 0$, which corresponds to the Fromm scheme.

3.4 Evaluation of the Diffusive Fluxes

With reference to Fig. 3.2 and with each unit normal in positive i, j or k direction, the discretization of the diffusive part of Eq. (3.8) may be written as:

$$
\begin{aligned}
\mathcal{F}^v_{ijk} = \frac{1}{Re}\Big\{ & \Big(\mathbf{f}^v_{i+\frac{1}{2}jk} n_{x_{i+\frac{1}{2}jk}} + \mathbf{g}^v_{i+\frac{1}{2}jk} n_{y_{i+\frac{1}{2}jk}} + \mathbf{h}^v_{i+\frac{1}{2}jk} n_{z_{i+\frac{1}{2}jk}}\Big)\Delta S_{i+\frac{1}{2}jk} \\
& - \Big(\mathbf{f}^v_{i-\frac{1}{2}jk} n_{x_{i-\frac{1}{2}jk}} + \mathbf{g}^v_{i-\frac{1}{2}jk} n_{y_{i-\frac{1}{2}jk}} + \mathbf{h}^v_{i-\frac{1}{2}jk} n_{z_{i-\frac{1}{2}jk}}\Big)\Delta S_{i-\frac{1}{2}jk} \\
& + \Big(\mathbf{f}^v_{ij+\frac{1}{2}k} n_{x_{ij+\frac{1}{2}k}} + \mathbf{g}^v_{ij+\frac{1}{2}k} n_{y_{ij+\frac{1}{2}k}} + \mathbf{h}^v_{ij+\frac{1}{2}k} n_{z_{ij+\frac{1}{2}k}}\Big)\Delta S_{ij+\frac{1}{2}k} \\
& - \Big(\mathbf{f}^v_{ij-\frac{1}{2}k} n_{x_{ij-\frac{1}{2}k}} + \mathbf{g}^v_{ij-\frac{1}{2}k} n_{y_{ij-\frac{1}{2}k}} + \mathbf{h}^v_{ij-\frac{1}{2}k} n_{z_{ij-\frac{1}{2}k}}\Big)\Delta S_{ij-\frac{1}{2}k} \\
& + \Big(\mathbf{f}^v_{ijk+\frac{1}{2}} n_{x_{ijk+\frac{1}{2}}} + \mathbf{g}^v_{ijk+\frac{1}{2}} n_{y_{ijk+\frac{1}{2}}} + \mathbf{h}^v_{ijk+\frac{1}{2}} n_{z_{ijk+\frac{1}{2}}}\Big)\Delta S_{ijk+\frac{1}{2}} \\
& - \Big(\mathbf{f}^v_{ijk-\frac{1}{2}} n_{x_{ijk-\frac{1}{2}}} + \mathbf{g}^v_{ijk-\frac{1}{2}} n_{y_{ijk-\frac{1}{2}}} + \mathbf{h}^v_{ijk-\frac{1}{2}} n_{z_{ijk-\frac{1}{2}}}\Big)\Delta S_{ijk-\frac{1}{2}}\Big\}
\end{aligned}
\tag{3.17}
$$

in which $\mathbf{f}^v_{i+\frac{1}{2}jk}$ is the mean value of $\mathbf{f}^v$ at the cell face $S_{i+\frac{1}{2}jk}$ etc. In order to calculate the mean diffusive flux vectors, approximations of the gradients ∇u, ∇v, ∇w and ∇T at each side of the hexahedron are required. These gradient vectors can be calculated with finite differences. A more robust approach is given by the replacement of the gradient operator by a surface integral expression following the Gauss theorem, the so-called "sub-block" method. According to the Gauss theorem we can write:

$$\iiint_V \nabla u \, dV = \iint_S u\mathbf{n}\, \mathrm{d}S \tag{3.18}$$

Consider for example the gradient $\nabla u_{i+\frac{1}{2}jk}$ at the cell face $S_{i+\frac{1}{2}jk}$ separating V_{ijk} and V_{i+1jk}, this gradient is approximated as a mean value over the intermediate "sub-block" or shifted cell $V_{i+\frac{1}{2}jk}$ (see Fig. 3.3) as:

$$\nabla u_{i+\frac{1}{2}jk} = \frac{1}{V_{i+\frac{1}{2}jk}} \oint_{S_{i+\frac{1}{2}jk}} u\mathbf{n}\, \mathrm{d}S \tag{3.19}$$

with $S_{i+\frac{1}{2}jk}$ the boundary of the shifted cell $V_{i+\frac{1}{2}jk}$ and $\mathbf{n}$ the outward unit normal. The surface

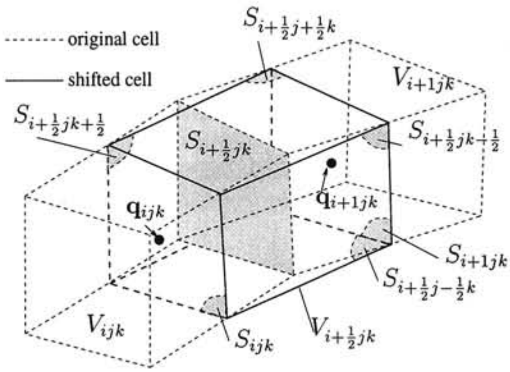

Figure 3.3: Shifted Finite Volume for Diffusive Flux Evaluation at $S_{i+\frac{1}{2}jk}$

integral for the shifted cell (Fig. 3.3) is approximated by:

$$\begin{aligned}\oint_{S_{i+\frac{1}{2}jk}} u\mathbf{n}\,\mathrm{d}S = \; & u_{i+1jk}\mathbf{n}_{i+1jk}\Delta S_{i+1jk} - u_{ijk}\mathbf{n}_{ijk}\Delta S_{ijk} \\ & + u_{i+\frac{1}{2}j+\frac{1}{2}k}\mathbf{n}_{i+\frac{1}{2}j+\frac{1}{2}k}\Delta S_{i+\frac{1}{2}j+\frac{1}{2}k} - u_{i+\frac{1}{2}j-\frac{1}{2}k}\mathbf{n}_{i+\frac{1}{2}j-\frac{1}{2}k}\Delta S_{i+\frac{1}{2}j-\frac{1}{2}k} \\ & + u_{i+\frac{1}{2}jk+\frac{1}{2}}\mathbf{n}_{i+\frac{1}{2}jk+\frac{1}{2}}\Delta S_{i+\frac{1}{2}jk+\frac{1}{2}} - u_{i+\frac{1}{2}jk-\frac{1}{2}}\mathbf{n}_{i+\frac{1}{2}jk-\frac{1}{2}}\Delta S_{i+\frac{1}{2}jk-\frac{1}{2}}\end{aligned} \tag{3.20}$$

in which the normal vectors and surfaces of the shifted cell faces are determined from the averages:

$$\begin{aligned}\mathbf{n}_{i+1jk} &= \tfrac{1}{2}\left(\mathbf{n}_{i+\frac{1}{2}jk} + \mathbf{n}_{i+\frac{3}{2}jk}\right) \\ \mathbf{n}_{ijk} &= \tfrac{1}{2}\left(\mathbf{n}_{i+\frac{1}{2}jk} + \mathbf{n}_{i-\frac{1}{2}jk}\right) \\ \mathbf{n}_{i+\frac{1}{2}j\pm\frac{1}{2}k} &= \tfrac{1}{2}\left(\mathbf{n}_{ij\pm\frac{1}{2}k} + \mathbf{n}_{i+1j\pm\frac{1}{2}k}\right) \\ \mathbf{n}_{i+\frac{1}{2}jk\pm\frac{1}{2}} &= \tfrac{1}{2}\left(\mathbf{n}_{ijk\pm\frac{1}{2}} + \mathbf{n}_{i+1jk\pm\frac{1}{2}}\right)\end{aligned} \tag{3.21}$$

and similar formulae are applied to the surfaces S_{i+1jk}, S_{ijk} etc. The variables u_{ijk}, u_{i+1jk} etc. are mean values of u at the corresponding shifted cell faces. The variables u_{ijk} and u_{i+1jk} at the cell faces S_{ijk} and S_{i+1jk} are the variables at the cell centers. The variables $u_{i+\frac{1}{2}j\pm\frac{1}{2}k}$ and $u_{i+\frac{1}{2}jk\pm\frac{1}{2}}$ are the average of the quantities in surrounding cell centers:

$$\begin{aligned}u_{i+\frac{1}{2}j\pm\frac{1}{2}k} &= \tfrac{1}{4}\left(u_{ij\pm1k} + u_{i+1j\pm1k} + u_{ijk} + u_{i+1jk}\right) \\ u_{i+\frac{1}{2}jk\pm\frac{1}{2}} &= \tfrac{1}{4}\left(u_{ijk\pm1} + u_{i+1jk\pm1} + u_{ijk} + u_{i+1jk}\right)\end{aligned} \tag{3.22}$$

Similar expressions are used for the gradients at the other cell faces. This diffusive flux computation is second order accurate for sufficiently smooth grids.

3.5 Boundary Treatment

The treatment of the boundary conditions is very consistent to the numerical flux calculations at the internal cell walls following the Osher scheme [15, 10]. This is a consequence of the fact that the Osher scheme is based on the Riemann invariants, which is also the case with a proper treatment of boundary conditions. The complete procedure is as follows. The flux at

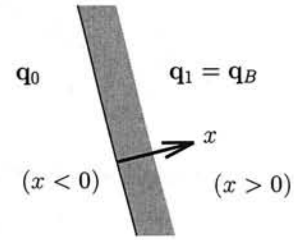

Figure 3.4: Boundary Treatment

the boundary of the domain will be determined partially by the state vector ($\mathbf{q}_0$ or $\mathbf{q}_1$) near the boundary and partially by the boundary conditions. Let us consider the case where the state $\mathbf{q}_1$ is the state at the boundary in a rotated Cartesian frame with the x-axis in a direction normal to the boundary surface (Fig. 3.4).

The first step is to determine the state vector $\mathbf{q}_B$ at the boundary, depending on $\mathbf{q}_0$ and the prescribed boundary conditions. Then the numerical flux function $\mathbf{f}_{NF}(\mathbf{q}_0\,,\mathbf{q}_B\,)$ gives the boundary flux vector. The following types of boundary conditions are used for the present computations:

Supersonic inflow: The state vector $\mathbf{q}_B$ is completely prescribed by the appropriate flow conditions.

Supersonic outflow: No boundary conditions have to be prescribed, thus $\mathbf{q}_B = \mathbf{q}_0$.

Solid wall: The solid wall is treated as a symmetry plane. In the case of an Euler flow simulation, only the velocity component normal to the wall is mirrored, the remaining quantities are copied:

$$u_B = -u_0 \;\; ; \;\; v_B = v_0 \;\; ; \;\; w_B = w_0 \;\; ; \;\; c_B = c_0 \;\; ; \;\; z_B = z_0$$

in which c and z are the speed of sound and a scaled entropy ($z = \ln p\rho^{-\gamma}$) respectively. Using this boundary treatment, it is guaranteed that for all numerical flux functions the boundary flux vector contains only a pressure term, $\mathbf{f}_{NF}\,(\mathbf{q}_0\,,\mathbf{q}_B\,) = (0\,,p_w\,,0\,,0\,,0)^T$.

In the case of a Navier-Stokes flow simulation, all velocity components are mirrored:

$$u_B = -u_0 \;\; ; \;\; v_B = -v_0 \;\; ; \;\; w_B = -w_0$$

The determination of the speed of sound c_B depends on the type of boundary condition prescribed for the temperature. For an adiabatic wall ($\partial T/\partial n = 0$) we use: $c_B = c_0$. When the temperature at the wall is prescribed, we use: $c_B = c_{wall} = \sqrt{\gamma(\gamma-1)T_{wall}}$, using the non-dimensionalization as described in section 3.1. The entropy z_B is obtained from the pressure p_B, which is equal to the pressure in the flow field p_0 assuming a zero pressure-gradient. This procedure has no consequences for the convective flux evaluation using the Osher or the Roe scheme. For the flux-splitting van Leer scheme, however, additional numerical dissipation is introduced. This additional dissipation is also apparent in the flow field, and is connected to the numerical scheme. Thus the boundary condition technique is consistent with the internal convective flux evaluation.

3.6 Multi-block Implementation

3.7 Solution Procedure

The system of nonlinear discretized equations is solved by means of a multigrid technique. Although not well-established for hyperbolic differential equations the multigrid technique has been applied successfully to the Euler equations [3, 15, 6]. The advantage of multigrid is that a convergence rate which is independent of the mesh size is achieved at quite general circumstances.

Consider the first- or second order accurate discretization of the Navier-Stokes equations given by equation Eq. (3.8) to be written as:

$$\Delta V_m \frac{\partial \mathbf{q}_m}{dt} + \mathcal{F}_m(\mathbf{q}_m) = 0 \tag{3.23}$$

where $\mathcal{F}_m$ is the spatial discretization operator at grid level m. A nested sequence of finite volume grids V_m $(m = 1, ..., n)$ is developed, with corresponding mesh sizes $h_1 > h_2 > ... > h_n$. Hence V_1 is the coarsest grid and V_n is the finest grid. The grids have a regular structure for reasons of simple implementation. Each finite volume on a given grid is the union of eight volumes on the next finer grid by skipping every other point in each direction on the finer grid.

The solution of the discretized equations is achieved by a nonlinear multigrid method (NMG), also known as full approximation scheme (FAS). In order to start with a good initialization, the NMG is preceded by a nested iteration. The nested iteration starts at the coarsest grid with an initial $\mathbf{q}_m$; $m = 1$. The approximate solution $\mathbf{q}_m$ is improved by a single NMG-cycle. The approximate solution $\mathbf{q}_{m+1}$ on the next finer grid is obtained by a prolongation of the approximate solution $\mathbf{q}_m$; this is achieved by a trilinear interpolation.

Within the multigrid, the solution at the different grid levels is smoothed by an implicit relaxation method. Implicit relaxation methods are unconditionally stable, and although the computational costs per iteration are higher, the overall performance may defeat an explicit time-integration method.

The smoothing procedure used here is based on an implicit time integration method. For the system of equations Eq. (3.23) a backward time-integration method can be written as:

$$\Delta V_j \frac{\Delta \mathbf{q}_j^{n+1}}{\Delta t} = -\mathcal{F}(\mathbf{q}_j^{n+1}) \tag{3.24}$$

where $\mathcal{F}(\mathbf{q}_j^{n+1})$ denotes the spatial discretization evaluated at time level $n+1$, and $\Delta\mathbf{q}_j^{n+1} = \mathbf{q}_j^{n+1} - \mathbf{q}_j^{n}$. Because Eq. (3.24) is a system of non-linear equations, this cannot be solved directly. Therefore a Newton linearization is used, which can be written as:

$$\mathcal{F}(\mathbf{q}_j^{n+1}) = \mathcal{F}(\mathbf{q}_j^{n}) + \left[\frac{\partial\mathcal{F}}{\partial\mathbf{q}}\right]_j^n \Delta\mathbf{q}_j^{n+1} \tag{3.25}$$

Substitution of Eq. (3.25) into Eq. (3.24) with $\mathcal{H} = \left[\dfrac{\partial\mathcal{F}}{\partial\mathbf{q}}\right]$ gives:

$$\left[\frac{\Delta V_j}{\Delta t} I - \mathcal{H}\right]_j^n \Delta\mathbf{q}_j^{n+1} = -\mathcal{F}(\mathbf{q}_j^{n}) \tag{3.26}$$

For the limit $\Delta t \to \infty$ Newton's root finding method is obtained, which should theoretically lead to quadratic convergence if the Jacobian matrix $\mathcal{H}$ is evaluated correctly. The system Eq. (3.26) represents a large banded block matrix, whose bandwidth is dependent on the order of accuracy of the spatial discretization and on the dimensions of the grid. Especially for the three-dimensional second-order discretized equations the bandwidth is very large. The construction of this matrix and solving the system requires an enormous amount of memory and CPU-time, which goes far beyond the capacities of most computers. Rather than solving Eq. (3.26) directly, a number of strategies have been developed in order to reduce the computational work, but maintaining a high convergence rate as far as possible. When second order accurate steady solutions are required, it is common practice to replace the true Jacobian matrix $\mathcal{H}$ in the left hand side of Eq. (3.26) by a much simpler matrix $\mathcal{H}^1$ based on the first-order accurate equations. For steady flows this has no effect on the accuracy of the right hand side discretization. The matrix for a three-dimensional first-order system is a septadiagonal block matrix, where the blocks itself are 5×5-matrices. However, certainly for three-dimensional problems this system is still too large to solve directly, so most implicit methods use iterative methods. In this report a Collective point Gauss-Seidel relaxation method has been used, with an ordering of the relaxation sweeps along diagonal planes in order to achieve some level of vectorization.

3.8 Numerical Simulation in the Current Investigation

The solution procedure described above has been applied in three different manners to calculate the flow field surrounding the FESTIP rocket model under investigation. The first type of numerical simulation used was based on the Euler equations and a structured mesh was applied. Thus the flow field was assumed to be non-viscous and non-heatconducting. Flow separation and the associated generation of vorticity is not modelled by the Euler equations. This might produce inaccuracies in the base region. The second type of numerical simulation used was based on the Navier-Stokes equations and a structured mesh was applied. In the base region and the jet region a stretching function has been used. Turbulence has not been taken into consideration, due to lack of a suitable turbulence model that will be able to simulate base flows. The mesh was not concentrated enough in the (laminar) boundary layers, however, since this type of simulation was mainly intended to provide a reference for the numerical Navier-Stokes simulation with mesh adaptation, this deficiency was not corrected. The third type of numerical simulation used was based on the Navier-Stokes equations and a mesh, adapted to the solution obtained through numerical Navier-Stokes simulation, was applied. Again turbulence has not been taken under consideration. Axi-symmetric simulation has been applied.

Chapter 4

MESH ADAPTATION

4.1 Introduction

Mesh generation has to provide an adequate resolution of the geometry of the flow domain and has to capture the flow features. In order to satisfy the latter requirement it is necessary to couple the mesh generation process with the flow algorithm. In mesh adaptation, the physics of the problem at hand must ultimately direct the mesh points to distribute themselves so that a functional relationship on these points can represent the physical solution with sufficient accuracy. The idea is to have the mesh points concentrating in regions of large variation in the physical solution. The mathematics controls the points by sensing the gradients in the physical solution. The points must concentrate, and yet no region can be allowed to become devoid of points. The distribution also must retain a sufficient degree of smoothness, and the mesh must not become too skewed, else the truncation error will be increased. It should be noted that the use of mesh adaptation might not necessarily increase computer time, even though more computations are necessary, since convergence properties of the solution may be improved, and certainly fewer points will be required. Interpolation must be used to transfer the values from the old mesh to the new mesh. In the following discussion, the problem of mesh adaptation will be formulated as a variational problem, the ideas being developed first in one dimension and then extended to multiple dimensions.

4.2 One-Dimensional Adaptation

4.2.1 Equidistribution

A number of studies of numerical solutions of boundary-value problems in ordinary differential equations have shown that the error can be reduced by distributing the mesh points so that some positive weight function, $w(x)$, is equally distributed over the field, i.e., in discrete form,

$$\Delta x_i w_i = constant \tag{4.1}$$

where Δx_i is the mesh interval, i.e. $x_{i+1} - x_i$. With this condition the mesh interval will be small where the weight function is large, and vice versa. Thus if the weight function is some measure of the error, or the solution variation, the mesh points will be closely spaced in regions of large error, or solution variation, and widely spaced where the solution is smooth.

4.2.2 Equidistribution by Transformation

The non-uniform point distribution can be considered to be a transformation, $x(\xi)$, from a uniform mesh in ξ-space, with the co-ordinate ξ serving to identify the mesh points. The mesh points are conveniently defined by successive integer values of ξ, making $\Delta\xi = 1$ by construction and the maximum value of ξ, i.e., N, equal to the total number of points on the line. Then $\Delta x = x_\xi \Delta\xi = x_\xi$, so that x_ξ represents the variation in x between mesh points. Hence the equidistribution statement can be represented as

$$x_\xi w(x) = constant \tag{4.2}$$

With the weight function w taken as a function of ξ this is the Euler equation for the minimization of the integral

$$I_1 = \int_0^1 w(\xi) x_\xi^2 d\xi \tag{4.3}$$

This follows from the calculus of variations, where the function x_ξ for which the integral $\int F(x, x_\xi) d\xi$ is an extremum is given by the solution of the differential equation $\frac{d}{d\xi}\frac{\partial F}{\partial x_\xi} - \frac{\partial F}{\partial x} = 0$. The latter equation is Euler's variational equation.

Since x_ξ represents the distance between mesh points, this variational problem can be interpreted as the minimization of the cumulative spacing between the mesh points in the least-squares sense, subject to the weight function $w(\xi)$. Implementation of this variational problem supplies the following differential equation for the mesh:

$$x_\xi w = \frac{L}{\int_1^N \frac{d\xi}{w}} \tag{4.4}$$

where L is the length of the mesh, which is a line in this case. This equation supplies an additional differential equation to be solved simultaneously with the differential equation system of the physical problem at hand, with the mesh point location x as an additional dependent variable, and ξ being taken as the independent variable.

An alternative viewpoint results from integrating over x, instead of over ξ, i.e., summing over the mesh intervals rather than over the mesh points. Since ξ identifies the mesh points, ξ_x represents the change in ξ, i.e., the number of mesh points per unit distance, and hence is the mesh point density. The equidistribution function is now the Euler equation for minimization of the integral

$$I_2 = \int_0^1 \frac{\xi_x^2}{w(x)} dx \tag{4.5}$$

Since ξ_x can be considered to represent the point density, this variational problem represents a minimization over the field of the density of mesh points in the least-squares sense, subject to the weight function, and thus produces the smoothest point distribution attainable. Implementation of this variational problem supplies the following differential equation for the mesh:

$$x_\xi w = \frac{1}{N-1} \int_0^L w dx \tag{4.6}$$

which supplies an additional differential equation to be solved simultaneously with the differential equation system of the physical problem at hand

4.2.3 Weight Functions

The effect of the weight function w is to reduce the point spacing x_ξ where w is large, and therefore the weight function should be set as some measure of the solution error, or as some measure of the solution variation. The simplest choice is just the solution gradient, i.e.,

$$w = u_x \tag{4.7}$$

In this case the equidistribution statement becomes

$$x_\xi u_x = constant \tag{4.8}$$

which then reduces to

$$u_\xi = constant \tag{4.9}$$

With the solution gradient as the weight function the point distribution adjusts so that the same change in the solution occurs over each mesh interval. This choice for the weight function has the disadvantage of making the spacing infinitely large where the solution is flat, however. A closely related choice, also based on the solution gradient, is the form

$$w = \sqrt{1 + u_x^2} \tag{4.10}$$

This results in an equidistribution statement as

$$x_\xi^2 + u_\xi^2 = constant \tag{4.11}$$

An increment of arc length, ds, on the solution curve u(x) is given by

$$ds = dx^2 + du^2 = (1 + u_x^2)dx^2 \tag{4.12}$$

so that this form of the weight function may be written as

$$w = s_x \tag{4.13}$$

In this case the equidistribution statement becomes

$$x_\xi s_x = constant \tag{4.14}$$

which then reduces to

$$s_\xi = constant \tag{4.15}$$

The mesh point distribution is such that the same increment in arc length on the solution curve occurs over each mesh interval. Unlike the previous choice, this weight function gives uniform spacing when the solution is flat. The concentration of points in the high-gradient region, however, is not as great. This concentration can be increased, while still maintaining uniform spacing where the solution is flat, by altering the weight function to

$$w = \sqrt{1 + \alpha^2 u_x^2} \tag{4.16}$$

This weight function involves a weighted average between the tendency toward equal spacing and that toward concentration entirely in the high-gradient regions. The larger the value of α, the stronger will be the concentration in the high-gradient regions and the wider the spacing in the flat regions.

A disadvantage of the above forms of the weight function is that regions near solution extrema, i.e., where $u_x = 0$ locally, are treated similar to flat regions. The distributions produced by the solution arc length forms would have closer spacings near the extrema, the effect is still the same, i.e., to concentrate points only near gradients, not extrema. Concentration near solution extrema can be achieved by incorporating some effect of the second derivative u_{xx} into the weight function. A logical approach is to include this effect through consideration of the curvature of the solution curve:

$$K = \frac{u_{xx}}{(1 + u_x^2)^{3/2}} \tag{4.17}$$

If the weight function is taken as

$$w = 1 + \beta^2 |K| \tag{4.18}$$

then points will be concentrated in regions of high curvature of the solution curve, e.g., near extrema, with a tendency toward equal spacing in regions of zero curvature, i.e., where the solution curve is straight. This weight function, however, has the serious disadvantage of treating high-gradient regions with little curvature essentially the same as regions where the curve is flat. A combination of the last two weight functions mentioned provides the desired tendency toward concentration both in regions of high-gradient and near extrema:

$$w = (1 + \beta^2 |K|) \sqrt{1 + \alpha^2 u_x^2} \tag{4.19}$$

where α and β are parameters to be specified.

Since the numerical evaluation of higher derivatives can be subject to considerable computational noise, the use of formal truncation error expressions as the weight function is usually not practical, hence the emphasis above on solution gradients and curvature.

For systems of equations involving more than one physical variable, one approach is to use the most rapidly varying or dominant physical variable in the definition of the weight function. Another is to use some average of the variations of the several variables. It is also possible to use entirely different meshes for different physical variables, with values transferred among the meshes by interpolation.

Of course, the proper choice of weight function depends on the goal that one wants to reach. A whole variety of weight functions is practicable.

4.3 Multi-Dimensional Adaptation

4.3.1 Adaptation Along Fixed Lines

In multiple dimensions, adaptation should in general occur in all directions in a mutually dependent manner. However, when the solution varies predominately in a single direction, one-dimensional adaptation of the forms discussed above can be applied with the mesh points constrained along one family of fixed curvilinear co-ordinate lines. The fixed family of lines is established by first generating a full multi-dimensional mesh by, for instance, elliptic or hyperbolic mesh generation systems, with the curvilinear co-ordinate lines of one family therein then being taken as the fixed lines. The points generated for this initial mesh, together with some interpolation procedure, serve to define the fixed lines along which the mesh points are constrained. The one-dimensional adaptation discussed above is then applied with x replaced by arc length along these lines.

4.3.2 Uncoupled Adaptation

One step beyond this one-dimensional adaptation along fixed lines is the application of successive one-dimensional adaptations separately in each of the curvilinear co-ordinate directions. This proceeds in the same manner as for the adaptation on the fixed lines, simply using the latest mesh to re-define the co-ordinate lines to serve as the 'fixed' lines in the next direction of adaptation.

4.3.3 Coupled Adaptation

The final mesh in the one-dimensional adaptation discussed above will, of course, be the result of the mesh point movement along the one family of fixed lines, and therefore the smoothness of the original mesh may not be preserved. Some restrictions on the point movement have generally been necessary in order to prevent excessive mesh distortion. In multiple dimensions it is generally desirable to couple the adaptation in the different directions in order to maintain sufficient smoothness in the mesh. One approach to such coupling is to generate the entire mesh anew at each stage of the adaptation from some basic mesh generation system, be it algebraic or based on partial differential equations. The structure of the mesh generation system serves to maintain smoothness in the mesh as the adaptation proceeds. This approach is analogous to the one-dimensional equidistribution discussed above.

4.3.4 Weight Functions

The one-dimensional weight function based on arc length on the solution curve can be generalized to higher dimensions as follows: Consider a hyperspace of dimensionality one greater than that of the physical space, with the solution, u, being the extra co-ordinate. Let the unit vector in the solution direction be e, this being orthogonal to the physical space. Then the position vector in this hyperspace is given by

$$\mathbf{R} = \mathbf{i}x + \mathbf{j}y + \mathbf{k}z + \mathbf{e}u = \mathbf{r} + \mathbf{e}u \tag{4.20}$$

where $\mathbf{r}$ is the position vector in physical space. Differential increments of arc length, surface, and volume, can be generated directly from the so-called covariant base vectors. Now the covariant metric element, denoted G_{ij}, in the hyperspace will be

$$G_{ij} = \mathbf{R}_{\xi i} \cdot \mathbf{R}_{\xi j} = (\mathbf{r}_{\xi i} + \mathbf{e}u_{\xi i}) \cdot (\mathbf{r}_{\xi j} + \mathbf{e}u_{\xi j}) = g_{ij} + u_{\xi i}u_{\xi j} \tag{4.21}$$

where g_{ij} is the metric element in physical space. With

$$u_{\xi i} = \nabla u \cdot bfr_{\xi i} \tag{4.22}$$

it can be shown that

$$\det |G_{ij}| = (1 + |\nabla u|^2) \det |g_{ij}| \tag{4.23}$$

In one dimension this reduces to the expression for arc length on the solution curve, in two dimensions it gives an expression for area on the solution surface. Thus the extension of the one-dimensional weight function base on arc length on the solution curve to two dimensions is that based on area on the solution surface:

$$w = \sqrt{1 + |\nabla u|^2} \tag{4.24}$$

4.4 Variational Approach

Considering the mesh from a continuous viewpoint, it occurs that something should be minimized by the mesh rearrangement, and thus a variational approach is logical. This is the natural extension of the equidistribution concept discussed above to multiple dimensions. Thus in general a weighted integral measure of the accumulation of some mesh property Q, either over the mesh points, i.e.,

$$I = \int wQd\xi \tag{4.25}$$

or over the physical field, i.e.,

$$I = \int wQd\mathbf{x} \tag{4.26}$$

where w is the weight function, will be minimized. The resulting Euler equations then will constitute the mesh generation system. There is no unique construction of the variational formulation for adaptive meshes, and this is an area that is not yet fully developed. Thompson [17] gives some constructions of the variational formulation that are logical and illustrative.

4.5 Distribution Functions

4.5.1 Introduction

Mesh generation for computational codes requires functions, which distribute points between given boundaries. In general, interpolation between $\mathbf{r}_1$ at $s = 0$ and $\mathbf{r}_2$ at $s = 1$ can be written as

$$\mathbf{r}(s) = \mathbf{r}_1 + f(s)(\mathbf{r}_2 - \mathbf{r}_1) \tag{4.27}$$

where $f(s)$ can be any function such that $f(0) = 0$ and $f(1) = 1$. A linear interpolation is obtained for $f(s) = s$. Another interpolation function often used ('stretching function') is the exponential function

$$f(s) = \frac{e^{s\beta} - 1}{e^{\beta} - 1} \tag{4.28}$$

where β is a parameter that can be adjusted to control the slope $df(s = 0)/ds$. According to Thompson [17] this function is not the best choice with regard to the truncation error affected by the point distribution. Therefore he recommends the use of functions based on the hyperbolic sine and tangent.

4.5.2 Hyperbolic Sine and Tangent Functions

Consider the function $f(s)$, where the arc length s varies from 0 to 1 as η varies from 0 to N, thus $s = \eta/N$. The spacing is specified at both ends by

$$\Delta f_1 = f(\eta = 1) - f(\eta = 0) \approx \frac{df(s = 0)}{ds}\frac{1}{N} \tag{4.29}$$

$$\Delta f_2 = f(\eta = N) - f(\eta = N - 1) \approx \frac{df(s = 1)}{ds}\frac{1}{N} \tag{4.30}$$

According to Thompson [17] the hyperbolic distribution function is constructed as follows. First we define

$$A = \frac{\sqrt{\Delta f_2}}{\sqrt{\Delta f_1}} \tag{4.31}$$

$$B = N\sqrt{\Delta f_1 \Delta f_2} \tag{4.32}$$

Then the following non-linear function is solved for δ, using a Newton linearization,

$$\frac{\sinh\delta}{\delta} = \frac{1}{B} \tag{4.33}$$

The distribution function is then given by

$$f(s) = \frac{u(s)}{A + (1 - A)u(s)} \tag{4.34}$$

where the function $u(s)$ is given by

$$u(s) = \frac{1}{2}\left\{1 + \frac{\tanh[\delta(s - \frac{1}{2})]}{\tanh\frac{\delta}{2}}\right\} \tag{4.35}$$

This function can be applied to a straight line between $\mathbf{r}_1$ and $\mathbf{r}_2$. The point locations $\mathbf{r}_\eta$ are given by

$$\mathbf{r}(\eta) = \mathbf{r}_1 + f(\eta/N)(\mathbf{r}_2 - \mathbf{r}_1) \qquad \eta = 0, 1, 2, ..., N \tag{4.36}$$

The parameter B is the ratio of the specified spacing to the linear spacing, $\Delta f_{eq} = 1/N$. If B is greater than 1, the hyperbolic functions all revert to circular functions.

The same procedure can also be used for a specified spacing at $s = 0$ or $s = 1$ only. For a given Δf_1 at $s = 0$, B is calculated from

$$B = N\Delta f_1 = \frac{\Delta f_1}{\Delta f_{eq}} \tag{4.37}$$

and Eq. (4.33) is solved for δ. The distribution function is then given by

$$f(s) = 1 + \frac{\tanh[\frac{1}{2}\delta(s - 1)]}{\tanh\frac{\delta}{2}} \tag{4.38}$$

This distribution function is shown in Fig. 4.1 for several values of B. With the spacing only

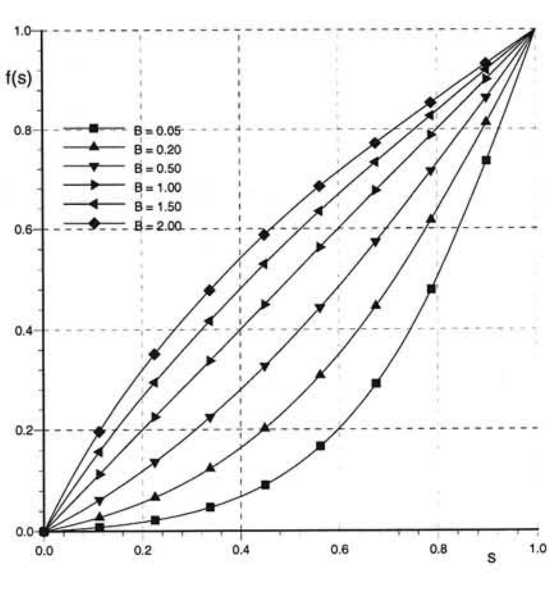

Figure 4.1: Distribution Function

specified at $s = 1$ ($\eta = N$) the procedure is the same, except that

$$B = N\Delta f_2 = \frac{\Delta f_2}{\Delta f_{eq}} \tag{4.39}$$

and Eq. (4.33) is solved for δ. The distribution function is then given by

$$f(s) = \frac{\tanh[\frac{1}{2}\delta s]}{\tanh\frac{\delta}{2}} \tag{4.40}$$

4.6 Utilization of Mesh Adaptation in the Current Investigation

4.6.1 Applied Method

The solution of the numerical simulation of the flow field surrounding the FESTIP rocket model varies predominately in a single direction, the radial direction. Therefore one-dimensional adaptation of the forms discussed above can be applied with the mesh points constrained along one family of fixed curvilinear co-ordinate lines, the so-called adaptation along fixed lines. The fixed family of lines is established by first generating a full mesh with the curvilinear co-ordinate lines of one family therein then being taken as the fixed lines. The points generated for this initial mesh, together with some interpolation procedure, serve to define the fixed lines along which the mesh points are constrained. The one-dimensional adaptation discussed above is then applied with x replaced by arc length along these lines.

4.6.2 Initial Mesh

The initial mesh is generated with the use of the hyperbolic sine and tangent distribution functions, as described above, in both the axial and the radial direction. A linear spacing, spacings at both ends, a spacing at $s = 0$, a spacing at $s = 1$, or a spacing at an interior point can be applied. The user can enter the value of the spacing and application method of spacing (linear spacing, spacings at both ends, et cetera). This option has been added to prevent possible deficiencies in the mesh. The grid spacing has to be defined for all four of the block boundaries. The initial mesh is then constructed using a transfinite interpolation. An example of an initial mesh constructed this way can be found in Fig. 4.2. The axial co-ordinate, i.e., x, has been transformed into the new co-ordinate χ and the radial co-ordinate, i.e., r, has been transformed into the new co-ordinate ζ. This can be seen in Fig. 4.3.

4.6.3 Adapted Mesh

The initial mesh serves to define the fixed lines along which the mesh points are constrained. Since the numerical solution varies predominately in the radial direction the lines along which the co-ordinate χ is constant define the fixed lines. The one-dimensional adaptation discussed

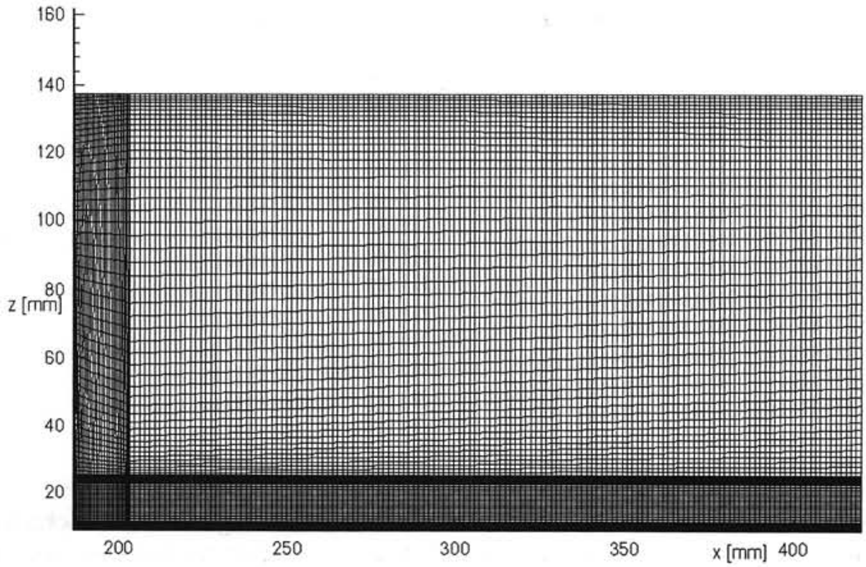

Figure 4.2: Example of the Initial Mesh

above is then applied with x replaced by arc length, which is defined by the co-ordinate ζ, along these lines.

The weight function to be used is some measure of the solution variation and the mesh points will be closely spaced in regions of large solution variation and widely spaced where the solution is smooth. Since the numerical evaluation of higher derivatives can be subject to considerable computational noise, the use of formal truncation error expressions as the weight function is usually not practical, hence the emphasis has been put on solution gradients.

For systems of equations involving more than one physical variable, one approach is to use the most rapidly varying or dominant physical variable in the definition of the weight function. In this case it has been made possible to use eight different physical variables to base the adaptation on: 1) the Mach number, 2) the dimension-less pressure, 3) the dimension-less Pitot-pressure, 4) the dimension-less temperature, 5) the dimension-less gas density, 6) the dimension-less total enthalpy, 7) the dimension-less total internal energy, and 8) the unscaled entropy. A numerical Navier-Stokes simulation has obtained these physical variables. The dominant physical variable in the present investigation is the Mach number. Therefore the Mach number has been used as variable in the definition of the weight function.

The weight function has been based upon solution gradients, taking into account the problems, which can occur where the solution is flat. The disadvantage is that the concentration of points in the high-gradient region is not tremendous.

Firstly a distribution function on the boundaries of the block is calculated. Then a distribution function in the inside of the block is calculated. The distribution functions are obtained by calculation of the weight function with the use of the physical variable obtained through numerical Navier-Stokes simulation. Finally these functions are used to generate the complete adapted

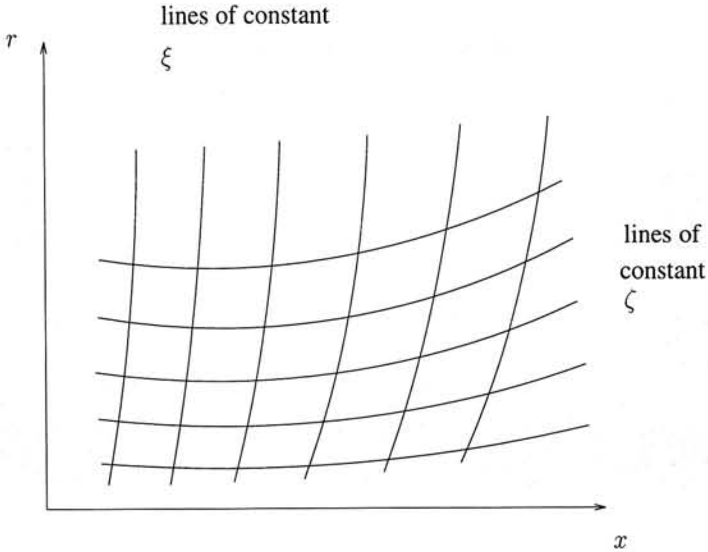

Figure 4.3: Co-ordinate Transformation Initial Mesh

mesh. An example of a Mach-adapted mesh constructed this way can be found in Fig. 4.4.

Applying all this to the mesh generating program itself, a procedure, as suggested by Starostin [16], is followed in which interpolation between $\mathbf{r}_1$ at $s = 0$ and $\mathbf{r}_2$ at $s = 1$ is be written as

$$\mathbf{r}(s) = \mathbf{r}_1 + \varphi(s)(\mathbf{r}_2 - \mathbf{r}_1) \tag{4.41}$$

where $\varphi(s)$ can be any function such that $\varphi(s) \in [0, 1]$. The derivative of the function $\varphi(s)$ is proportional to the derivative of the physical variable distribution. To obtain such a relationship a new function is introduced

$$P(s_i) - P(s_{i-1}) = |var(s_i) - var(s_{i-1})| \qquad i = 0, 1, 2, ..., N \tag{4.42}$$

where $var(s)$ represents the physical variable at point s. The effect of this function can be seen in Fig. 4.5. This function is then normalized such that $P(s) \in [0, 1]$ applies for $s \in [0, 1]$. In this way a normalized increasing physical variable distribution has been created.

To obtain the proportionality of the function $\varphi(s)$ to the derivative of the physical variable distribution the latter distribution is used in the equation

$$Q(s) = \frac{P(s) + W\xi(s)}{1 + W} \quad ; \quad Q(s) \in [0, 1] \tag{4.43}$$

where $\xi(s)$ is a smooth, continuously increasing mathematical function such that $\xi(s)\ in[0, 1]$. An example of this function can be seen in Fig. 4.6. In the procedure used a distribution function as described in previous sections is utilized for $\xi(s)$.

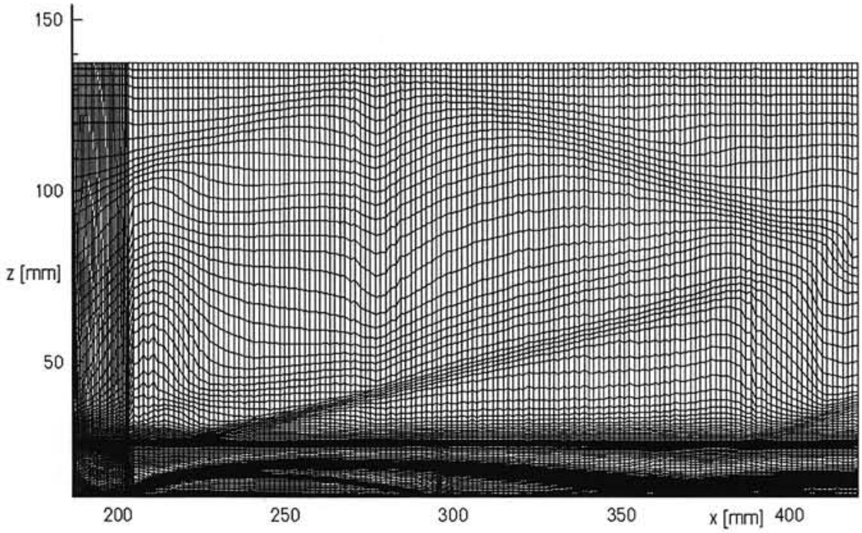

Figure 4.4: Example of the Adapted Mesh

W is a weight factor such that $W \in [0, \infty >$. The function $Q(s)$ provides a relation to the solution gradient and a distribution function. If $W = 0$ then the function $Q(s)$ equals the normalized physical variable distribution, whereas if W is infinitely large $Q(s)$ equals the (distribution) function $\xi(s)$.

The function $Q(s)$ can now be used as the function $\varphi(s)$ in Eq. (4.41) and an interpolation between $\mathbf{r}_1$ at $s = 0$ and $\mathbf{r}_2$ at $s = 1$ can be applied where the solution gradient and the distribution function determine the distribution of the mesh points.

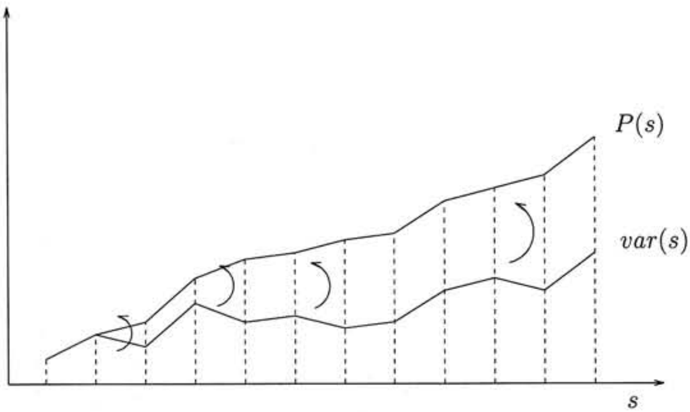

Figure 4.5: Example of the Function P(s)

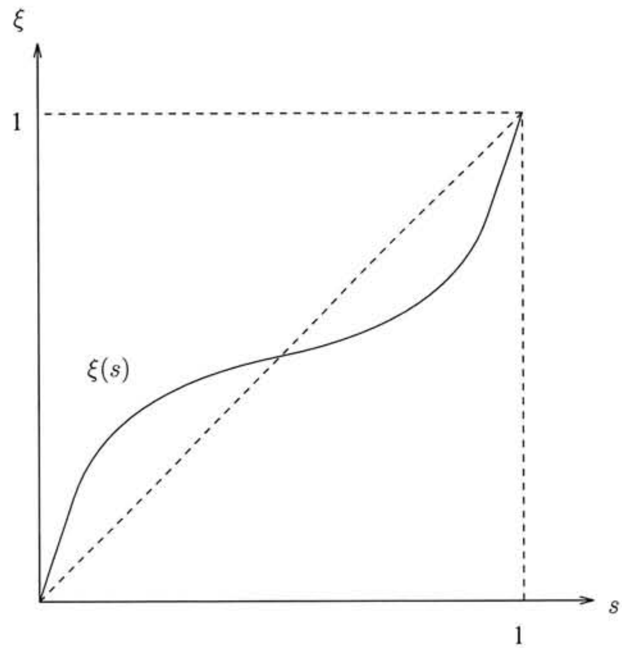

Figure 4.6: Example of the Function $\xi(s)$

Chapter 5

RESULTS OF THE NUMERICAL SIMULATION

5.1 Introduction

Both Euler and laminar Navier-Stokes computations have been performed, because it was questioned whether or not specific governing equations and specific mesh generating techniques provided a better physical representation of the flow field. The object was to obtain an accurate physical representation of the flow field in order to be able to compare numerical results with experimental results [4, 14]. A three- dimensional view of the numerical model can be seen in Fig. 5.1.

The first type of numerical simulation used was based on the Euler equations and a non-adapted structured mesh was used. Thus the flow field was assumed to be non-viscous and non- heat-conducting. The second type of numerical simulation used was based on the Navier- Stokes equations and a structured mesh, stretched in the base and jet region, was applied. Turbulence has not been taken into consideration. The mesh was not concentrated enough in the boundary layers, which was not corrected because this type of simulation was mainly intended to provide a reference for the numerical Navier-Stokes simulation with mesh adaptation. The third type of numerical simulation used was based on the Navier-Stokes equations and a mesh, adapted to the solution obtained by a numerical Navier-Stokes simulation, was applied. Again turbulence has not been taken into account.

For the numerical simulation the emphasis was put on the Mach number distribution. The free stream Mach number was kept at $M_\infty = 2.98$ and the ratio of jet stagnation pressure to free stream static pressure $N = p_{tj}/p_\infty$ ranged from $p_{tj}/p_\infty = 600$ to no-jet flow. Subsequently, a comparison can be made between the results of the numerical simulations and the experimental results.

For each series of simulations a comparison will be made between the meshes used. The convergence of the different types of simulation will be looked at as well. Through means of flooded Mach-number contour plots the results of the numerical simulations will be compared. A good description of the streamline patterns in the base flow is important, because heat- conduction results as a consequence of reattachment of the flow to the base of the model. This is mainly of importance in the case of hot jets. In the present investigation a cold jet is considered, however, streamlines in the base region will be examined in order to study possible reattachment. Because of lack of experimental data concerning the circulation, the accuracy of the streamline patterns

Figure 5.1: 3-D View of the Numerical Model

can not be validated. Finally the base pressure distribution will be considered for comparison with experimental data.

5.2 Numerical Method

Only axi-symmetric simulations have been applied. The mesh consisted of eight blocks, including a block in the interior of the nozzle of the model; in this way, parallel computing was possible. The tunnel wall has also been simulated using solid wall boundary conditions for the Euler equations.

A second order accurate spatial discretization was used in combination with the Van Leer scheme. Computations were carried out until a convergence of at least three orders of magnitude was reached.

5.3 Flow Quantities

At the free stream Mach number of $M_\infty = 2.98$, the free stream static pressure was predetermined at $p_\infty = 0.1618$ bar and the free stream temperature at $T_\infty = 165.58$ K, for all the numerical simulations. The free stream static pressure and temperature were obtained from previous experiments at $M_\infty = 2.98$. With the specific gas constant for air of $R = 287.05$ and a ratio of specific heats $\gamma = c_p/c_v = 1.4$, using the perfect gas relationship, the free stream density and speed of sound become $\rho = 0.3405kg/m^3$ and $a = \sqrt{\gamma RT} = 257.96m/s$, respectively. For the Euler simulations the Reynolds number was set at infinity. For the Navier-Stokes simulations the Reynolds number based on the model length was in the order of $5 \cdot 10^6$.

5.4 Boundary Conditions

The boundary conditions for the numerical Euler simulations consisted of prescribing a supersonic inflow with the free stream flow quantities and an angle of attack of zero degrees, and prescribing a supersonic outflow. The conditions in the nozzle were such that an exit Mach number of $M = 4$ could be reached. Conditions in the settling chamber of the nozzle were subsonic; at the inflow the total pressure, total temperature and flow direction were prescribed. The Mach number, static pressure and static temperature are determined by the solution procedure and the area ratio of the inflow and the throat of the jet. The model itself and the tunnel wall were assumed to be solid walls. Furthermore, an axis of symmetry was defined.

The boundary conditions for the numerical Navier-Stokes simulations were the same as for the Euler simulations, except for the model itself, which was assumed to be an adiabatic wall, with a no-slip condition prescribed.

5.5 No Jet-Flow

5.5.1 Mesh

The meshes used for the different types of numerical simulation are shown in Fig. 5.2. In all cases a concentration of mesh points behind the model has been applied in order to capture the shear layer as good as possible. For the Navier-Stokes simulation a concentration of mesh points at the walls of the base has been applied. At the boundary layers along the model the mesh is similar to the mesh used for the Euler simulation, which is not suitable for boundary layer calculation. A concentration of mesh points in this area is needed for the Navier-Stokes simulation to capture the boundary layers. This concentration is absent and the boundary layers are not captured accurately.

The mesh adapted to the Mach number distribution generated by the Navier-Stokes simulation shows a clear contraction of mesh points in the shear layer. The boundary layer along the model is also accurately captured. The mesh points at the base of the model are distributed to capture the circulation as good as possible. The shock wave system, generated by the model itself, is also captured. Note the capture of the reflecting shock wave at the tunnel wall.

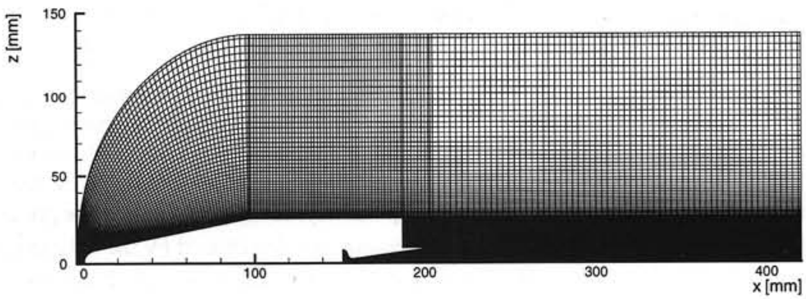

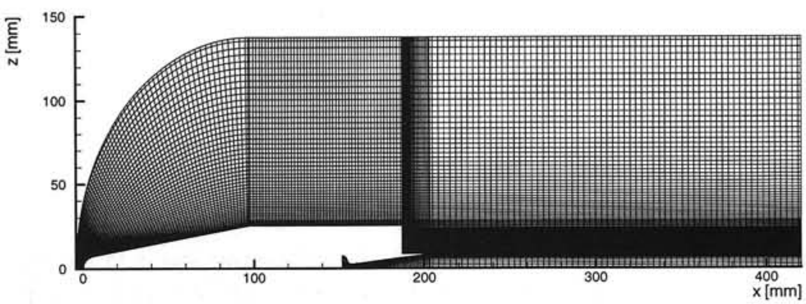

(b) Navier-Stokes Simulation

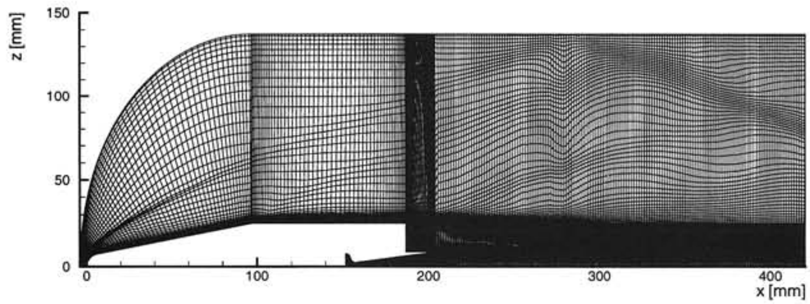

(c) Navier-Stokes, Mach-adapted Mesh
Figure 5.2: Mesh, $M_\infty = 2.98$, No-jet

5.5.2 Convergence

The convergence plots of the different types of numerical simulation are shown in Fig. 5.3. All three of the simulations converge well. However, the Navier-Stokes simulation needs roughly twice as much iterations as the Euler simulation to converge properly. The Mach-adapted mesh is responsible for increasing the number of iterations by approximately a factor two.

5.5.3 Mach Number Contour Plots

The Mach number plots of the different types of numerical simulation are shown in Fig. 5.4. Clearly visible are the compression waves coming from the conical forebody of the model and reflecting on the tunnel walls, the expansion fans emanating from the end of afterbody, the shear layers and the circulation region behind the model.

In case of the Euler simulation, which should be inviscid, the circulation region downstream of the base is confined to a relatively small area in comparison with the Navier-Stokes simulations. The maximum Mach number is about 5% higher than for the Navier-Stokes simulations. The maximum Mach number does not exceed the free stream Mach number overwhelmingly. The simulation is not trustworthy in the base region, because flow separation and the associated generation of vorticity is not modelled correctly by the Euler equations. The attachment of the shear layer to the model is not in conformity with reality. The circulation area is not captured as well by the numerical Euler simulation as it is by the numerical Navier-Stokes simulations, as may be evident by comparison with experimental results.

The initial Navier-Stokes simulation does not capture the boundary layers very well. Furthermore, the shear layers are larger than for the simulation using the Mach-adapted mesh. The latter clearly provides better results in these areas, because the mesh points are more concentrated in these areas than for the initial Navier-Stokes simulation. However, special attention

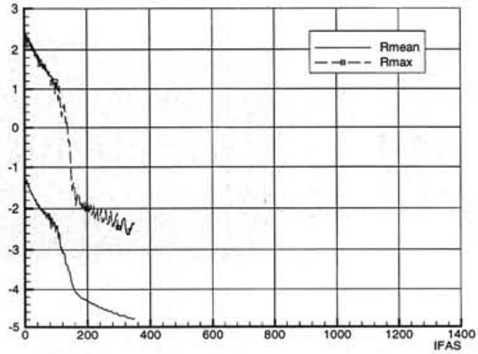

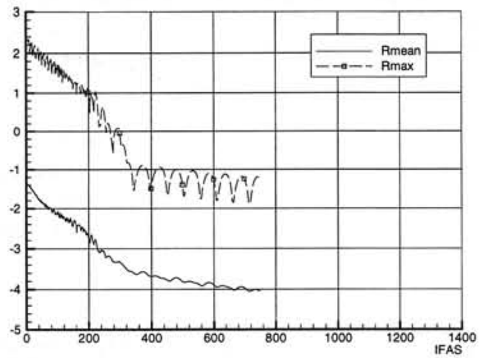

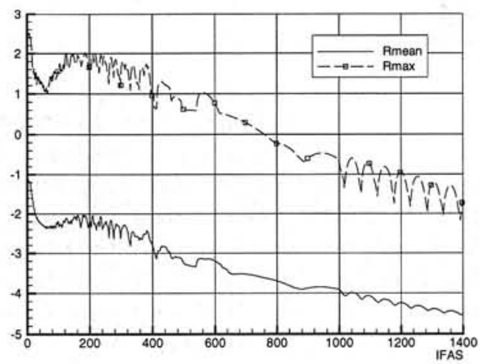

(c) Navier-Stokes, Mach-adapted Mesh

Figure 5.3: Convergence Plot, $M_\infty = 2.98$, No-jet

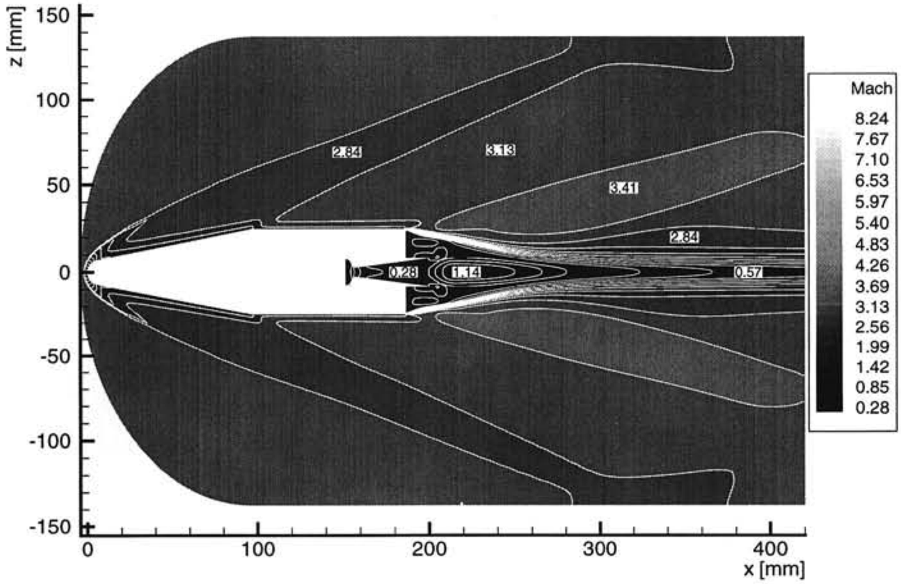

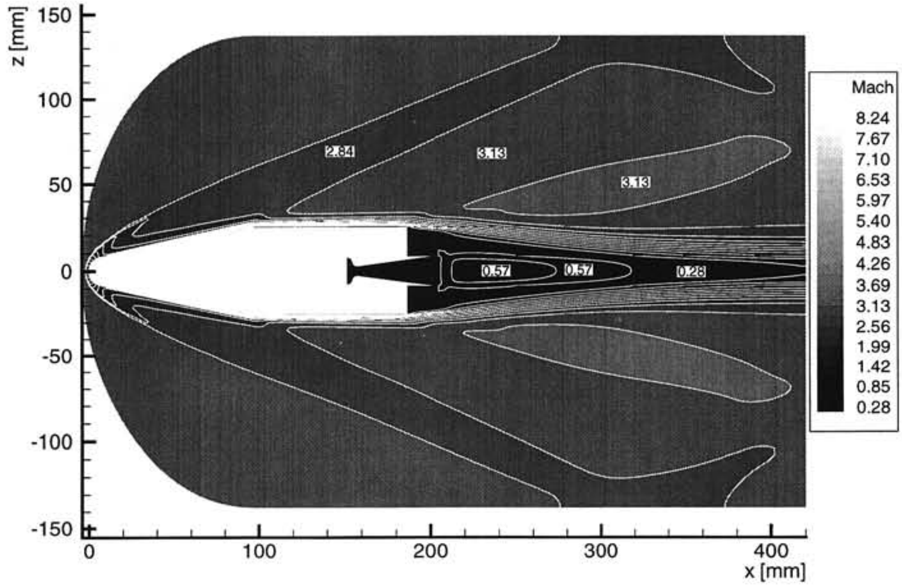

(b) Navier-Stokes Simulation

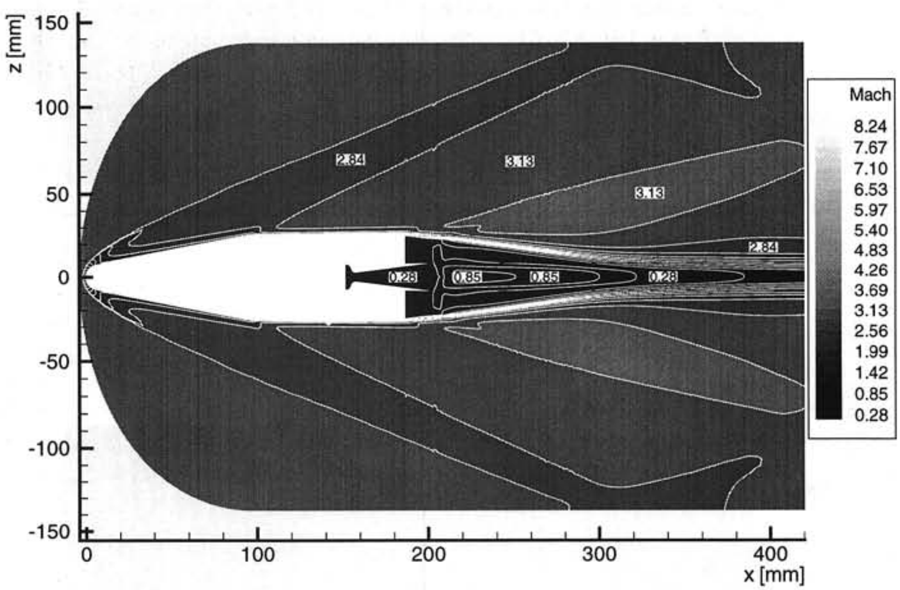

(c) Navier-Stokes, Mach-adapted Mesh

Figure 5.4: Mach Number Contour Plot, $M_\infty = 2.98$, No-jet

has to be given to possible introduction of unwanted pseudo-physical effects. Constructing the adapted mesh with care can prevent this introduction. In the current investigation the adapted mesh was constructed such that at the axis of symmetry sufficient smoothness had been acquired. However, the transition of the base region to the region behind the nozzle should have been smoother; at this point the non-adapted mesh may provide better results. The simulation using the Mach-adapted mesh provides a good conformity with reality. The circulation region provides physically interesting results (see section 5.5.4). The solution obtained by the Navier-Stokes simulation using a Mach-adapted mesh has been used for comparison with experimental results.

5.5.4 Streamlines

The streamline plots obtained through the numerical Navier-Stokes simulation using a Mach-adapted mesh are shown in Fig. 5.5. Fig. 5.5a gives a general overview of the complete flow field, whereas Fig. 5.5b shows the region of circulation. In the case of no-jet there are three different circulation areas within the complete circulation region. Two relatively small circulation areas occur at the base of the model. The outer one, and the smallest, is rotating in the clockwise direction. The inner one, and the larger, is rotating counter-clockwise. Reattachment of the flow to the base of the model is possible at the transition at the base from one circulation area to the other and seems to occur at approximately $z = 11mm$, at 44% of the base radius, measured from the centerline. The third circulation area, and by far the largest, is located downstream of the nozzle of the model and is rotating in a clockwise direction. At the nozzle, reattachment of the flow seems to occur at the transition from the second mentioned to the third mentioned circulation area, at approximately $x = 193mm$. However, in both cases reattachment can not be accurately visualized. The co-flowing supersonic stream feeds the third mentioned circulation area. In turn, this large circulation area feeds the counter-clockwise rotating circulation area. Ultimately, the latter feeds the small, clockwise rotating circulation area, which feeds the co-flowing supersonic stream in return. The total mass flow to the cavity must be zero.

5.5.5 Base Pressure

The base pressure plots of the different types of numerical simulation are shown in Fig. 5.6 together with the experimental data of FESTIP Aerothermodynamics [4] investigation. The boundary of the model base is located at $z = 25mm$. Both for the Euler simulation and Navier-Stokes simulation with regular mesh the influence of the relatively high pressure in the expansion fan reaches beyond this boundary. For the Navier-Stokes simulation with Mach-adapted mesh this transition is more in agreement with reality. For the FESTIP Aerothermodynamics [4] investigation steady base pressure measurements were conducted. Under conditions similar to the present investigation an average dimension-less base pressure of $p_b/p_\infty = 0.32$ was measured. Furthermore the base pressure seemed to be nearly constant along radial lines.

Keeping the above-mentioned facts in mind it can be deducted that the base pressure plot generated by the numerical Euler simulation is not in correspondence with reality. The base pressure is not constant and the average value of approximately $p_b/p_\infty = 0.41$ is too high. The Navier-Stokes simulation with regular mesh is even worse in agreement with reality. The Navier-Stokes

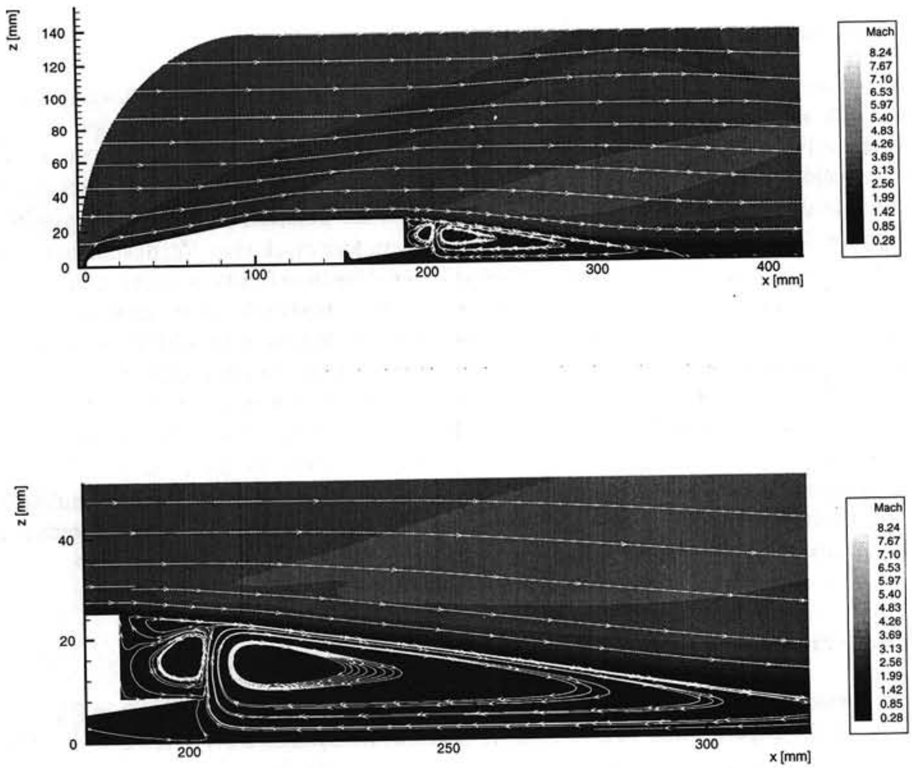

(b) Navier-Stokes Simulation, Mach-adapted Mesh, BaseJet Region

Figure 5.5: Streamlines, $M_\infty = 2.98$, No-jet

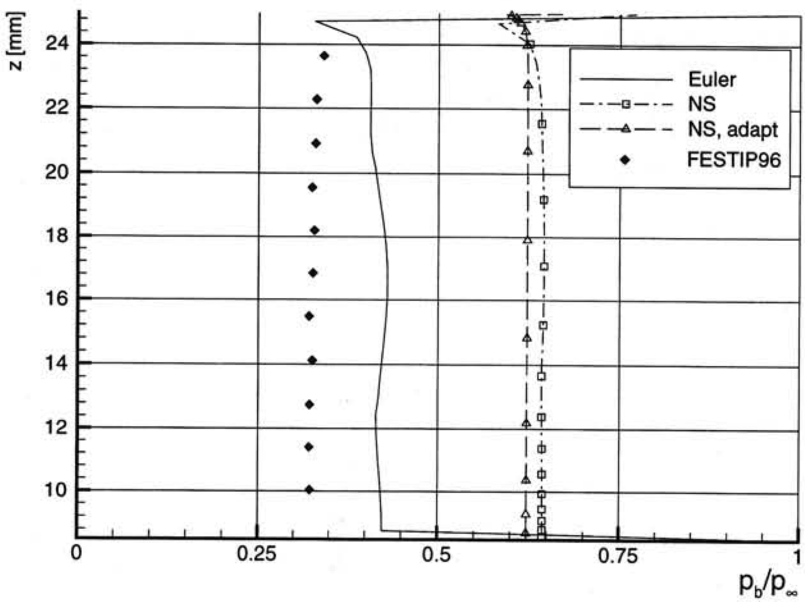

Figure 5.6: Base Pressure, $M_\infty = 2.98$, No-jet

simulation with Mach-adapted mesh does not have the flaws mentioned before. The base pressure is nearly constant, but the average value of upwards of $p_b/p_\infty = 0.62$ is in very bad agreement with reality. It seems that the Euler simulation provides the most accurate value of base pressure, but that the physical behaviour is best captured by the Navier-Stokes simulation with Mach-adapted mesh. Nevertheless, no accurate prediction has been made.

5.6 Jet-Flow, $N = p_{tj}/p_\infty = 115$

5.6.1 Mesh

The meshes used for the different types of numerical simulation are shown in Fig. 5.7. Concentration of mesh points behind the model has been applied for all three types of simulation in order to capture the jet region as good as possible. For the Navier-Stokes simulation a concentration of mesh points at the walls of the base has been applied. At the boundary layers along the model the mesh is similar to the mesh used for the Euler simulation, which is not equipped for the computation of boundary layers. However, to capture the boundary layers, a concentration of mesh points in this area is needed for the Navier-Stokes simulation. The boundary layers are not captured accurately, because this concentration is absent.

The mesh adapted to the Mach number distribution generated by Navier-Stokes simulation, shows a clear contraction of mesh points at the shear layer, jet boundary, and barrel shock. The boundary layer along the model is also accurately captured. The mesh points at the base of the model are distributed to capture the circulation as good as possible. The shock wave system (note the capture of the reflecting shock wave at the tunnel wall), generated by the model itself, is also captured.

5.6.2 Convergence

The convergence plots of the different types of numerical simulation are shown in Fig. 5.8. All three simulations converge well and considerably faster than in the case of no-jet. The Navier-Stokes simulation needs roughly two times as much iterations as the Euler simulation to converge properly. The Mach-adapted mesh is responsible for increasing the number of iterations by approximately a factor two.

5.6.3 Mach Number Contour Plots

The Mach number plots of the different types of numerical simulation are shown in Fig. 5.9. Visible are the compression waves coming from the conical forebody of the model and reflecting on the tunnel walls, the expansion fans emanating from the end of afterbody, the shear layers, the jet boundary, the barrel shock and the circulation region at the base of the model. The jet causes a substantial rise in maximum Mach number in the base region. The core flow accelerates to a high Mach number.

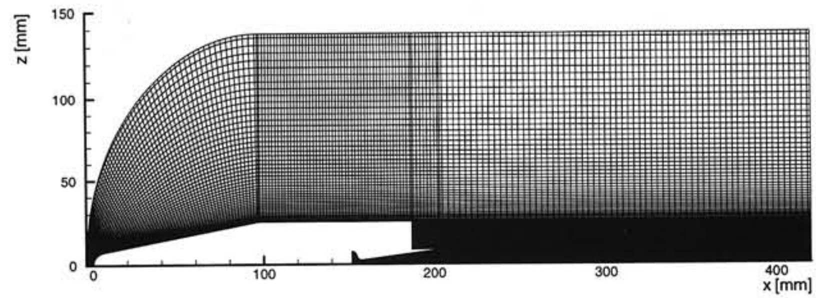

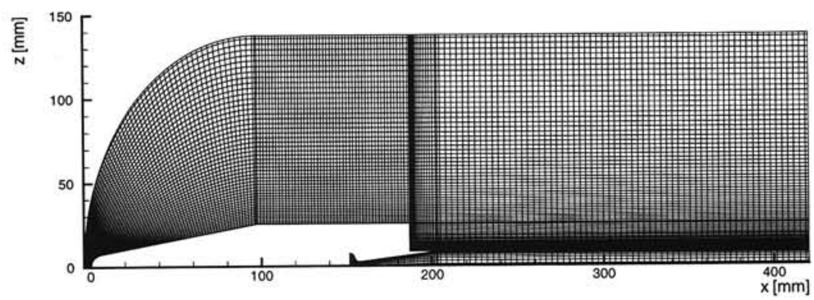

(b) Navier-Stokes Simulation

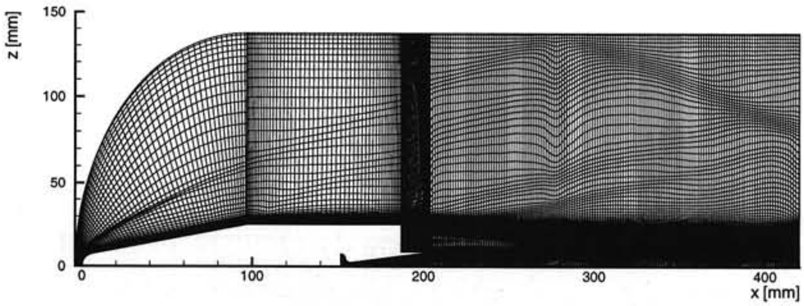

(c) Navier-Stokes, Mach-adapted Mesh

Figure 5.7: Mesh, $M_\infty = 2.98$, $p_{tj}/p_\infty = 115$

In case of the Euler simulation the circulation region again is confined to a relatively small area at the base in comparison with the Navier-Stokes simulations. Also, as in the case of no-jet, the attachment of the shear layer to the base of the model is not in accordance with reality. Experimental results indicate that the circulation area is not captured as well by the Euler simulation as by the Navier-Stokes simulations.

The Navier-Stokes simulations show a better conformity with reality, although the initial Navier-Stokes simulation doesn't capture the boundary layers very well. The simulation using the Mach-adapted mesh clearly provides better results. The plume core is also more accurately portrayed, which can be seen from the barrel shock and the reflection of the barrel shock. Moreover, the tendency to dampen the formation of downstream shock cells is not clearly portrayed by the Euler simulation and the Navier-Stokes simulation with regular mesh. The simulation using the Mach-adapted mesh provides an accurate reproduction of the physical flow field brought forth by the interaction of the jet and the co-flowing stream. However, as mentioned before, possible introduction of pseudo- physical effects has to be taken care of. This introduction can be prevented by careful construction of the adapted mesh. In the current investigation the adapted mesh was constructed so that at the axis of symmetry sufficient smoothness had been acquired. Nevertheless, the gain in accuracy in the circulation region and the jet region is extensive. The simulation using the Mach-adapted mesh provides a good conformity with reality. The solution obtained by the Navier-Stokes simulation using a Mach-adapted mesh has been used for comparison with experimental results.

5.6.4 Streamlines

The streamline plots of the numerical Navier-Stokes simulation using a Mach-adapted mesh are shown in Fig. 5.6.4. Fig. 5.6.4a gives a general overview of the entire flow field, and Fig. 5.6.4b shows the base and jet region. The jet boundary is characterized by a concentration of stream-

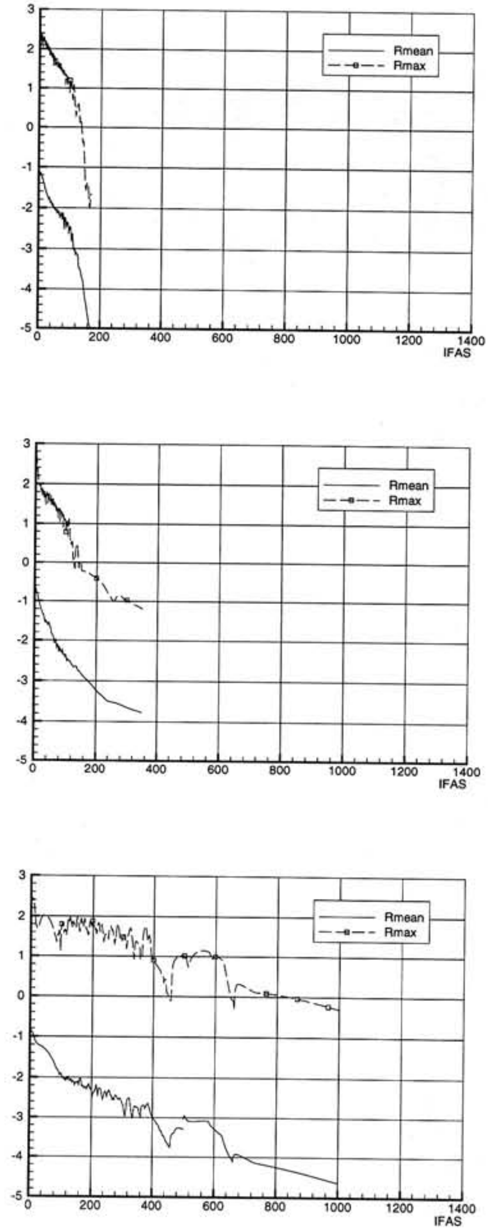

(c) Navier-Stokes, Mach-adapted Mesh

Figure 5.8: Convergence Plot, $M_\infty = 2.98$, $p_{tj}/p_\infty = 115$

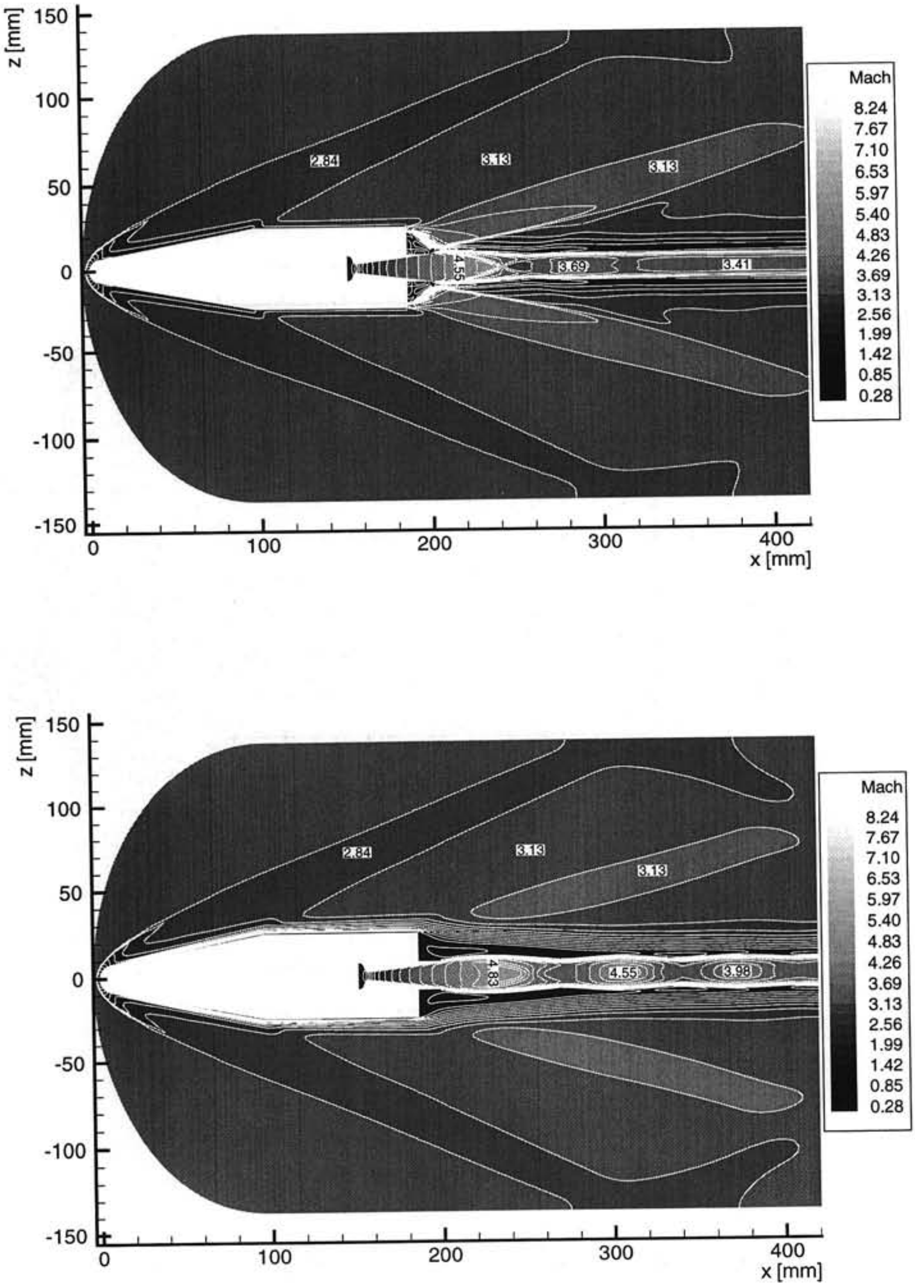

(b) Navier-Stokes Simulation

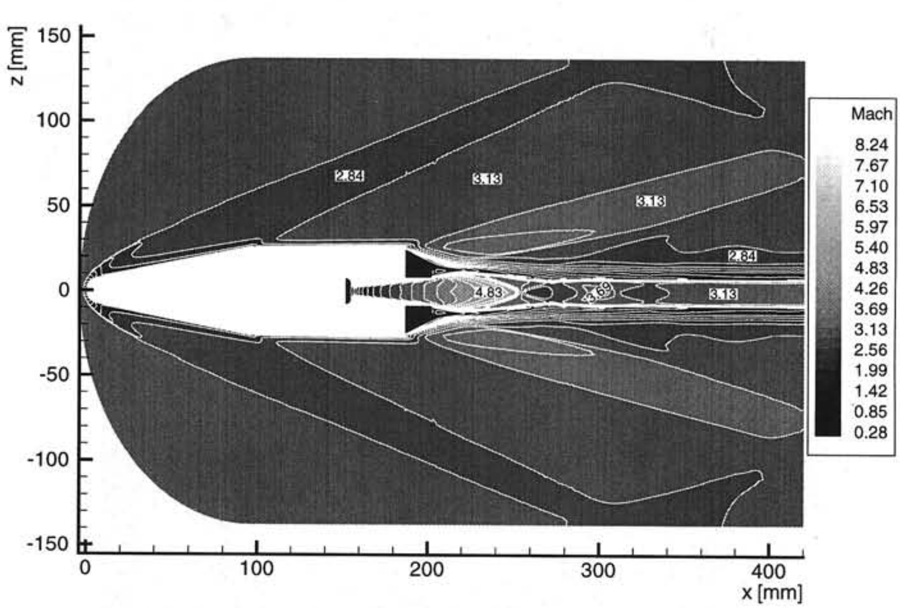

(c) Navier-Stokes, Mach-adapted Mesh

Figure 5.9: Mach Number Contour Plot, $M_\infty = 2.98$, $p_{tj}/p_\infty = 115$

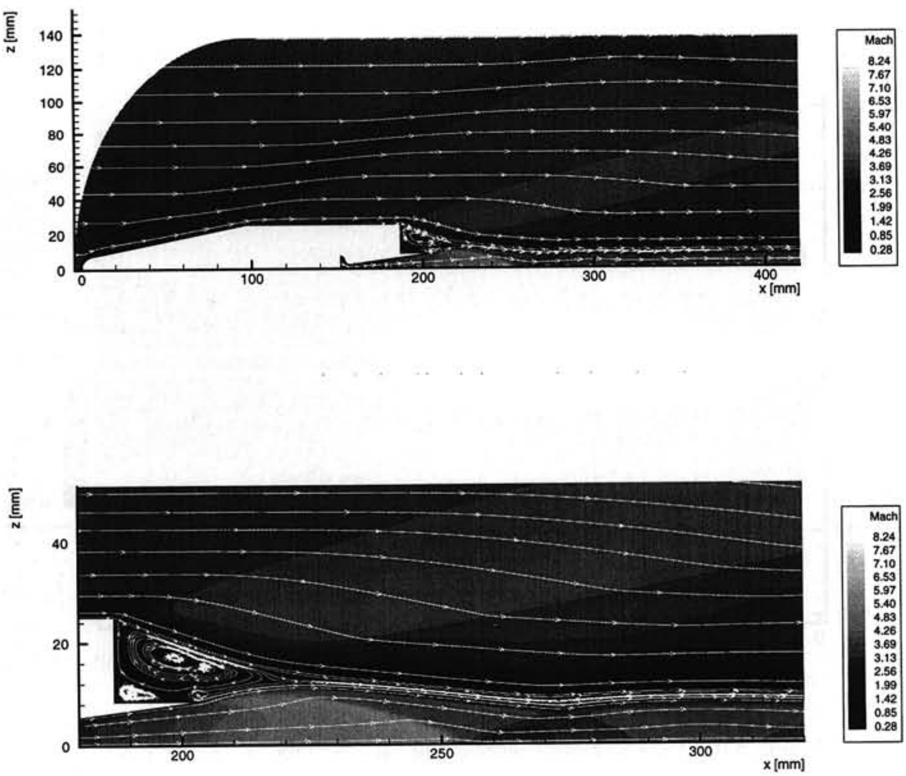

(b) Navier-Stokes Simulation, Mach-adapted Mesh, BaseJet Region

Figure 5.10: Streamlines, $M_\infty = 2.98$, $p_{tj}/p_\infty = 115$

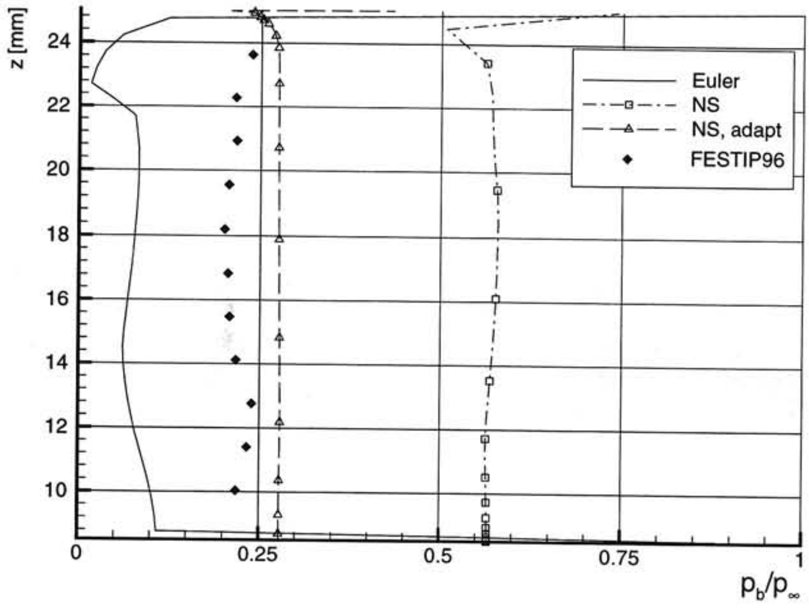

Figure 5.11: Base Pressure, $M_{\infty} = 2.98$, $p_{tj}/p_{\infty} = 115$

lines. Contrary to the no-jet case, there are only two different circulation areas within the complete circulation region at the base, which are both subdivided into two regions with centred vortices. At the outer part of the base region a relatively large circulation area occurs, where two vortices are rotating in clockwise direction. The area is dominated by the big vortex nearest to the base. At the inner part of the base region the second circulation area is located. Here, two vortices are rotating in counter-clockwise. Reattachment of the flow to the base seems to occur at approximately $z = 12mm$, at 48% of the base radius (measured from the centerline), but can not be visualized properly. The circulation area at the outer part of the base region feeds the shear layer and the counter-clockwise rotating circulation area. The latter then feeds the jet boundary. As a result of this complicated flow a net mass flow from the jet is 'filling' the cavity. Subsequently, the same mass flow is taken away from the cavity by the external flow, because the total mass flow to the cavity must be zero.

5.6.5 Base Pressure

The base pressure distributions of this jet-pressure case are shown in Fig. 5.11. The influence of the relatively high pressure in the expansion fan reaches beyond the model base boundary both for the Euler simulation and Navier-Stokes simulation with regular mesh. The attachment of the shear layer to the model, in case of the Euler simulation, is located below the edge of the model base, causing the transition to the 'base pressures' to occur at a radial distance, which is too low. For the Navier-Stokes simulation with Mach-adapted mesh the transition to the 'base pressures' is more conform reality. Under conditions similar to the present investigation, in [4] an average dimension-less base pressure of $p_b/p_\infty = 0.21$ was measured, nearly constant along radial lines.

The base pressure obtained with the Euler simulation has an average value of approximately $p_b/p_\infty = 0.08$, which is too low as compared to experimental results. The Navier-Stokes simulation with regular mesh gives an average value of approximately $p_b/p_\infty = 0.57$, which is too high. Besides, the transition to the 'base pressures' still occurs at a radial distance that is too low. The Navier-Stokes simulation with Mach-adapted mesh yields a base pressure that is nearly constant, but the average value of almost $p_b/p_\infty = 0.28$ is still not in agreement with experiments. Although the pressures are off by some 30%, the Navier- Stokes simulation with Mach-adapted mesh still captures the physical behaviour the best. Nevertheless, as in the case of no-jet, no accurate prediction could be made. However, in this case the base pressure calculation is better.

5.7 Jet-Flow, $N = p_{tj}/p_\infty = 200$

5.7.1 Mesh and Convergence

The meshes for the different types of numerical simulation in this case are shown in Fig. 5.12; they are similar, with regard to their construction, to those used in the case of $N = p_{tj}/p_\infty = 115$. However, the mesh adapted to the Mach number shows a clearer contraction of mesh points at the shear layer, jet boundary, and barrel shock. In addition the concentration of mesh points at the compression waves, resulting from the interaction of the reflected barrel shock and the shear layer, is visible.

As may be seen from Fig. 5.13 all simulations converge well, similar to the case of $N = p_{tj}/p_\infty = 115$. Again, the Navier-Stokes simulation needs roughly twice as much iterations as the Euler simulation to converge properly. The Mach-adapted mesh is responsible for increasing the number of iterations by approximately a factor three.

5.7.2 Mach Number Contour Plots

In the Mach number plots, shown in Fig. 5.14, again the compression and expansion waves are well visualized. The Mach number distribution shows a further increase in magnitude because of the tremendous acceleration of the core flow.

Also for $N = p_{tj}/p_\infty = 200$ the circulation region is, in case of the Euler simulation, confined to a relatively small area at the base compared to the Navier-Stokes simulations. The simulation using the Mach-adapted mesh portrays the plume core accurately, which may be observed in Fig. 5.14c from the barrel shock and the reflection of the barrel shock. This simulation provides an accurate reproduction of the interacting flow fields. The compression waves, resulting

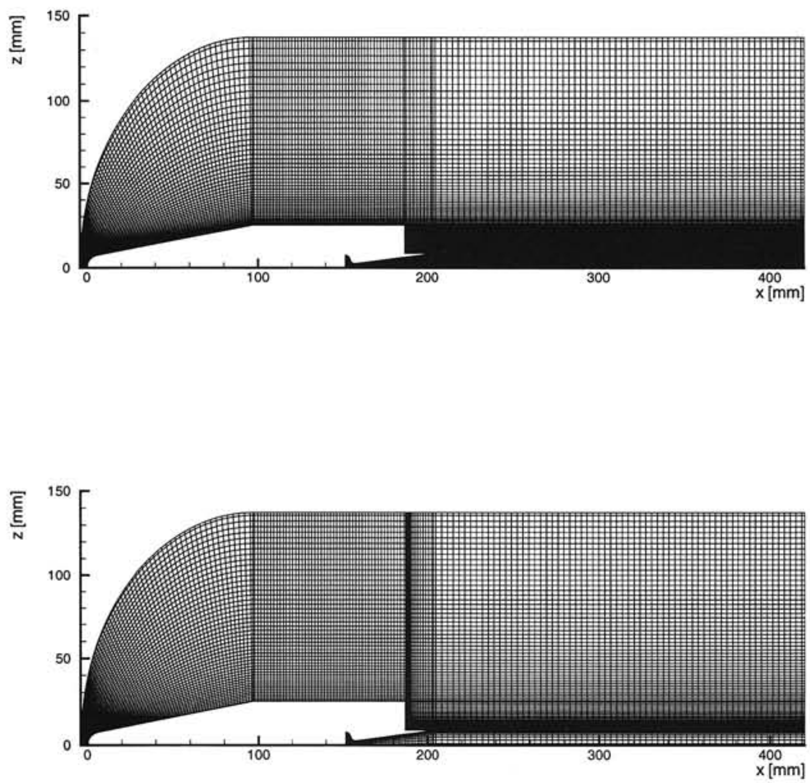

(b) Navier-Stokes Simulation

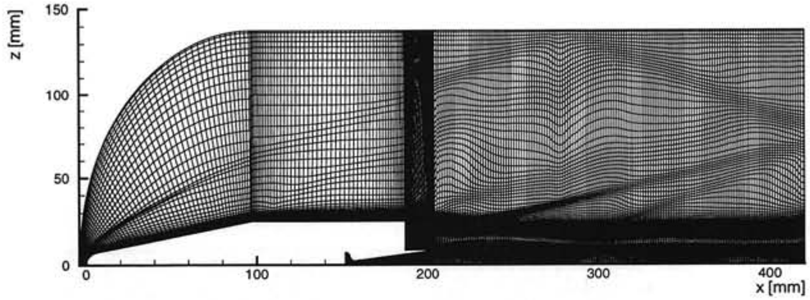

(c) Navier-Stokes, Mach-adapted Mesh

Figure 5.12: Mesh, $M_\infty = 2.98$, $p_{tj}/p_\infty = 200$

from the interaction of the reflected barrel shock and the shear layer, are reproduced well with similar interesting physics. As in the previous cases, possible introduction of pseudo-physical effects has been prevented by careful construction of the adapted mesh.

5.7.3 Streamlines and Base Pressure

The streamlines for the Mach-adapted mesh are given in Fig. 5.15. Fig. 5.15a gives a general overview, the base and jet region is shown in Fig. 5.15b. The two different circulation areas, as shown in the case of $N = p_{tj}/p_\infty = 115$, within the complete circulation region at the base have not been altered substantially. In contrary to the case of $N = p_{tj}/p_\infty = 115$ the latter circulation area seems to have three centres of vorticity.

The base pressure plots of this case are shown in Fig. 5.16. The boundary of the base is located at $z = 25mm$. The FESTIP experiments [4] for this case gave an average dimension-less base pressure of $p_b/p_\infty = 0.23$.

The average base pressure, for the Euler computations, of approximately $p_b/p_\infty = 0.08$ is too low. The Navier-Stokes simulation with regular mesh gives too high an average value of approximately $p_b/p_\infty = 0.36$. The Navier-Stokes Mach-adapted mesh simulation shows a nearly constant base pressure with an average value slightly above $p_b/p_\infty = 0.31$, still not in agreement with the experiments.

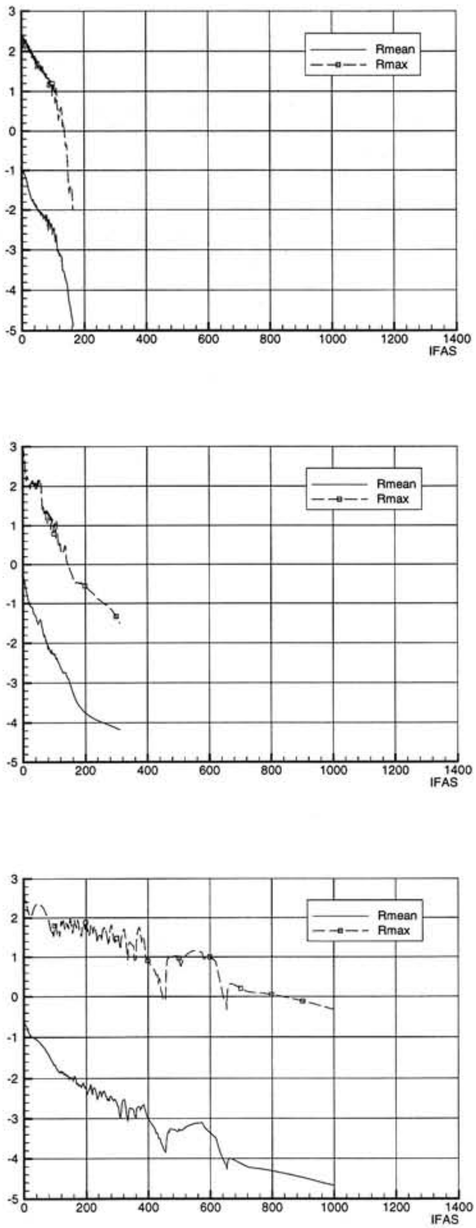

(c) Navier-Stokes, Mach-adapted Mesh

Figure 5.13: Convergence Plot, $M_\infty = 2.98$, $p_{tj}/p_\infty = 200$

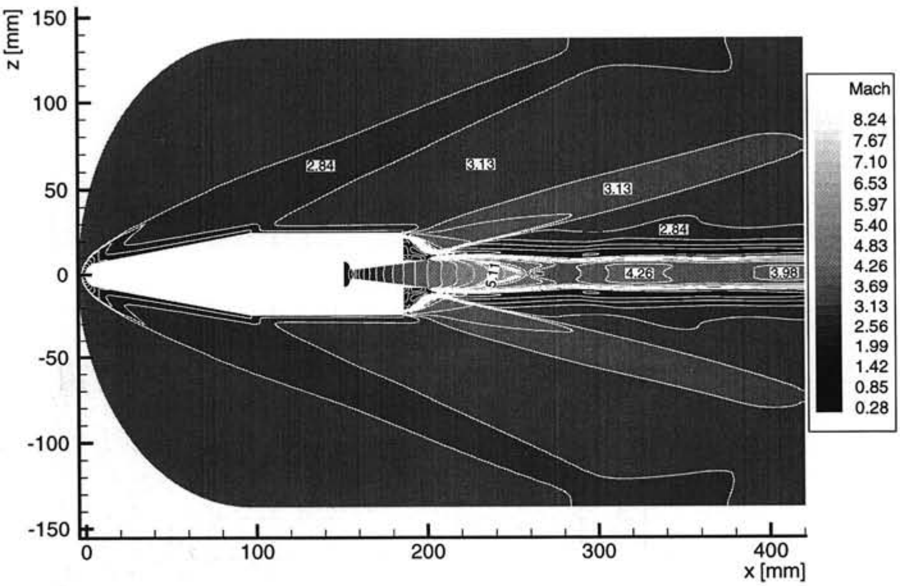

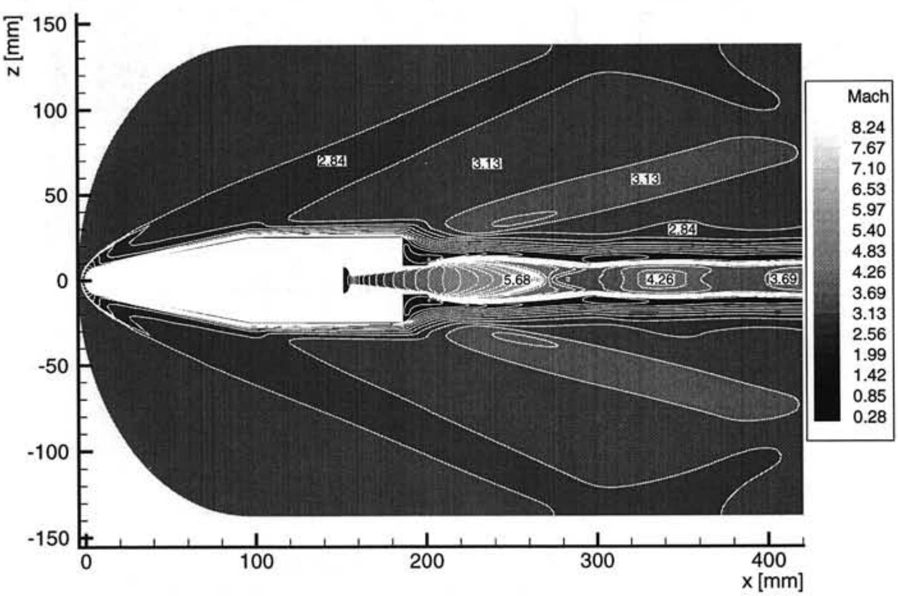

(b) Navier-Stokes Simulation

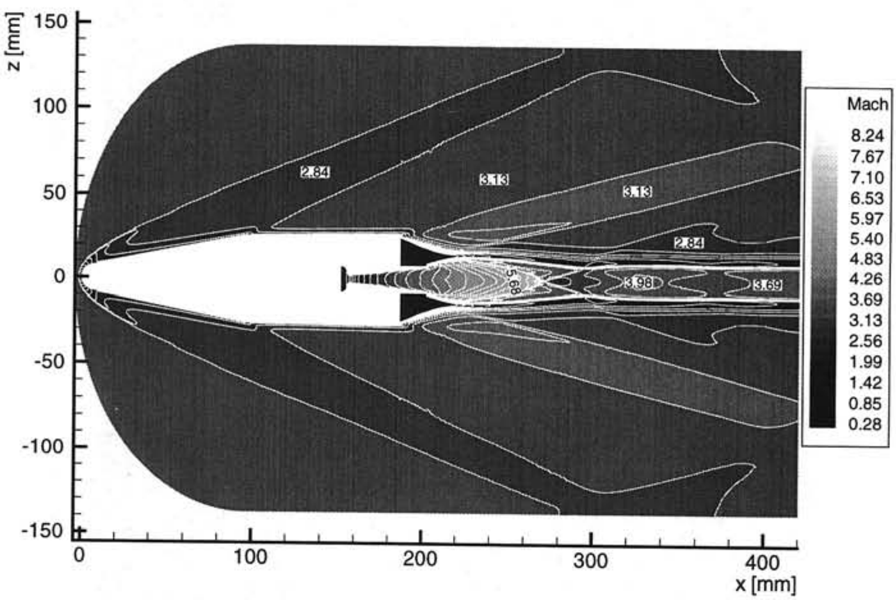

(c) Navier-Stokes, Mach-adapted Mesh

Figure 5.14: Mach Number Contour Plot, $M_\infty = 2.98$, $p_{tj}/p_\infty = 200$

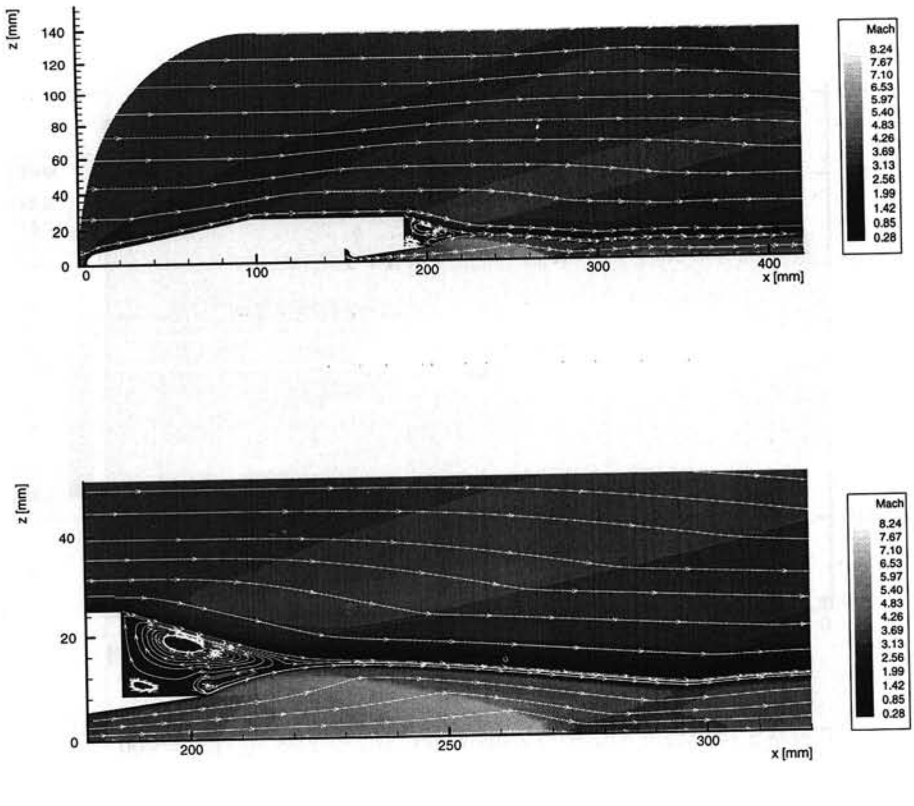

(b) Navier-Stokes Simulation, Mach-adapted Mesh, BaseJet Region

Figure 5.15: Streamlines, $M_\infty = 2.98$, $p_{tj}/p_\infty = 200$

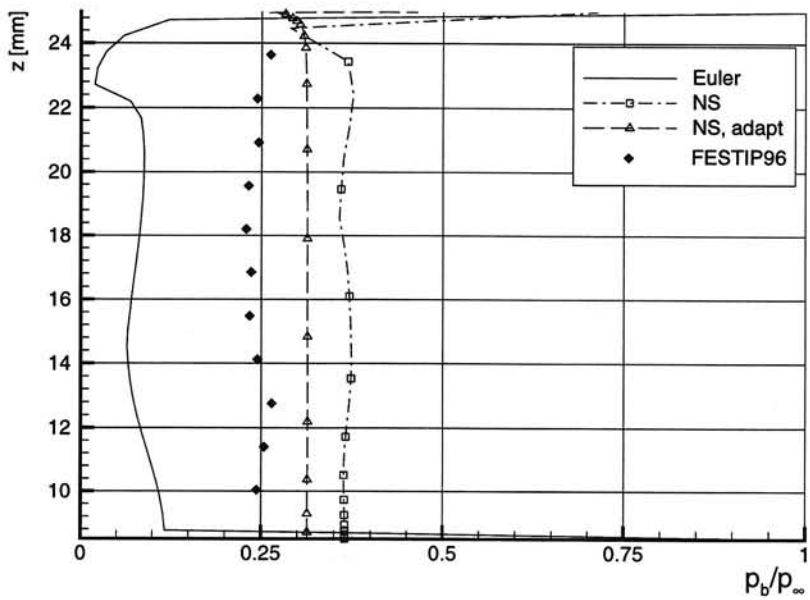

Figure 5.16: Base Pressure, $M_\infty = 2.98$, $p_{tj}/p_\infty = 200$

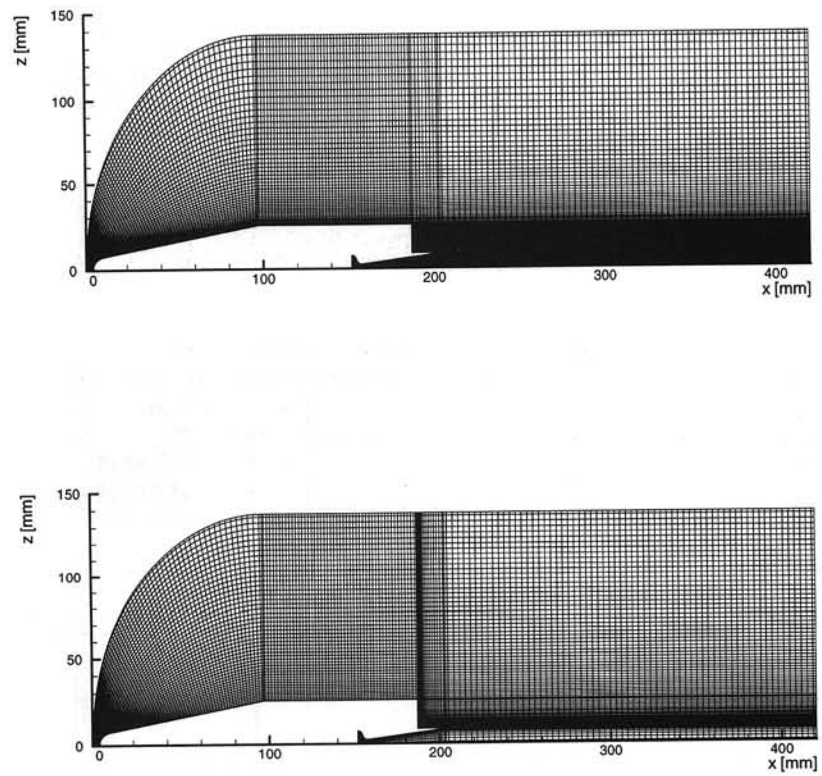

(b) Navier-Stokes Simulation

5.8 Jet-Flow, $N = p_{tj}/p_\infty = 400$

5.8.1 Mesh and Convergence

The meshes, which are similar in construction to the two previous jet-pressure cases, are shown in Fig. 5.17. The phenomena depicted are the same as for the case of $N = p_{tj}/p_\infty = 200$.

In the convergence plots of Fig. 5.18 it may be observed that, in contradiction to the two previous jet-pressure cases, the Navier-Stokes simulation with regular mesh converges roughly as fast as the Euler simulation. Also, the convergence of the Navier- Stokes simulation with Mach-adapted mesh needs slightly more iterations than in the two previous cases and the solution converges with a bit more difficulty.

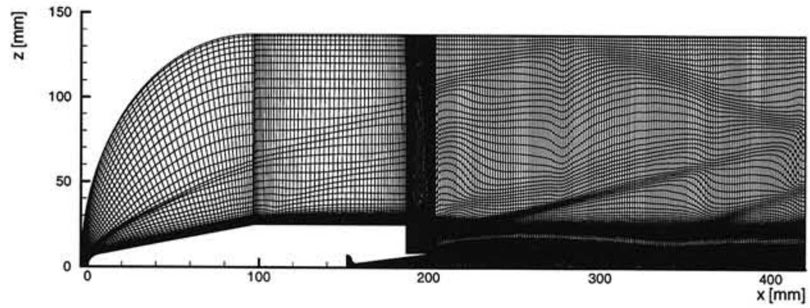

(c) Navier-Stokes, Mach-adapted Mesh
Figure 5.17: Mesh, $M_\infty = 2.98$, $p_{tj}/p_\infty = 400$

5.8.2 Mach Number Contour Plots

Fig. 5.19 shows the Mach number plots at these conditions. The occurring phenomena are quantitatively the same as in the foregoing cases with jet, except that the plume cells are even more elongated. The comments made previously may be repeated here.

5.8.3 Streamlines and Base Pressure

Fig. 5.20 shows streamline plots of the Navier-Stokes simulation using a Mach-adapted mesh. No basic difference in the streamline pattern occurs when comparing to the cases of $N = p_{tj}/p_\infty = 115$ and $N = p_{tj}/p_\infty = 200$. In this case, reattachment of the flow to the base seems to occur at approximately 49% of the base radius.

The base pressure plots of the different types of numerical simulation are displayed in Fig. 5.21. For this case in the FESTIP Aerothermodynamics [4] investigation an average base pressure of $p_b/p_\infty = 0.29$ was measured, nearly constant along radial lines. For the numerical Euler simulation, the base pressure at an average value of approximately $p_b/p_\infty = 0.07$ is too low. The average value of roughly $p_b/p_\infty = 0.36$ generated by the Navier-Stokes simulation with regular mesh is too high. Moreover, it has the same value as for the $N = p_{tj}/p_\infty = 200$ case. Also for the Navier-Stokes simulation with Mach- adapted mesh a base pressure of $p_b/p_\infty = 0.34$ is not much different from the previous $N = p_{tj}/p_\infty = 200$ case. Compared to the measured data the base pressures produced with the Mach-adapted mesh are still off by some 20%. Although this numerical simulation represents the physics of the flow the best, no accurate quantitative predictions are possible.

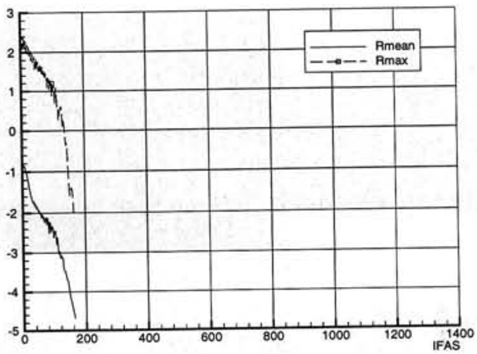

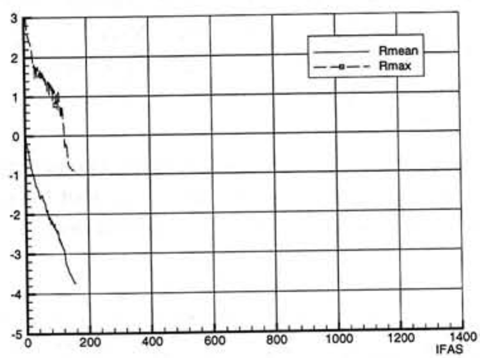

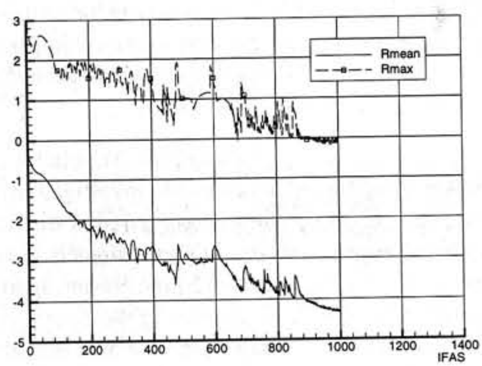

(c) Navier-Stokes, Mach-adapted Mesh

Figure 5.18: Convergence Plot, $M_\infty = 2.98$, $p_{tj}/p_\infty = 400$

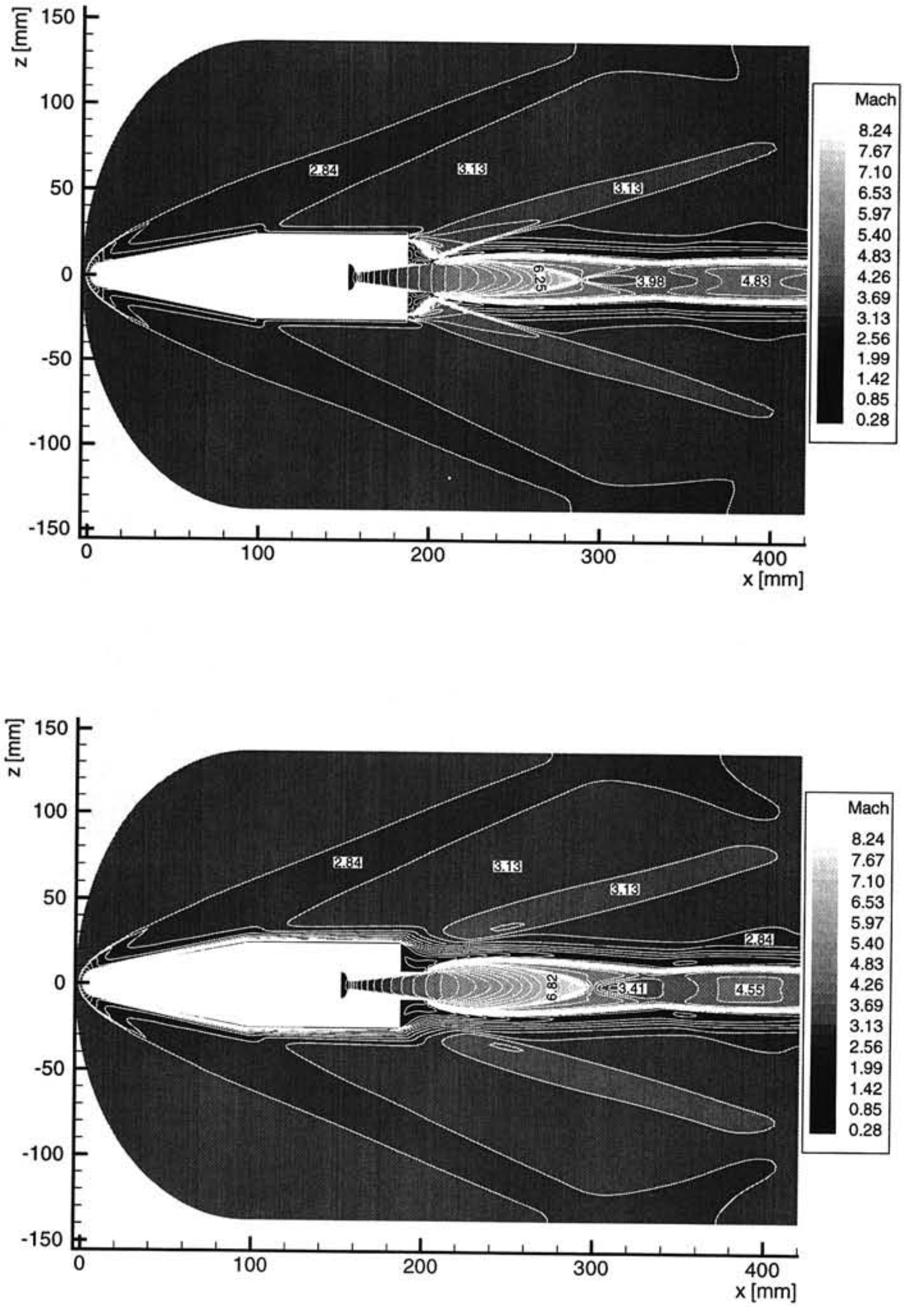

(b) Navier-Stokes Simulation

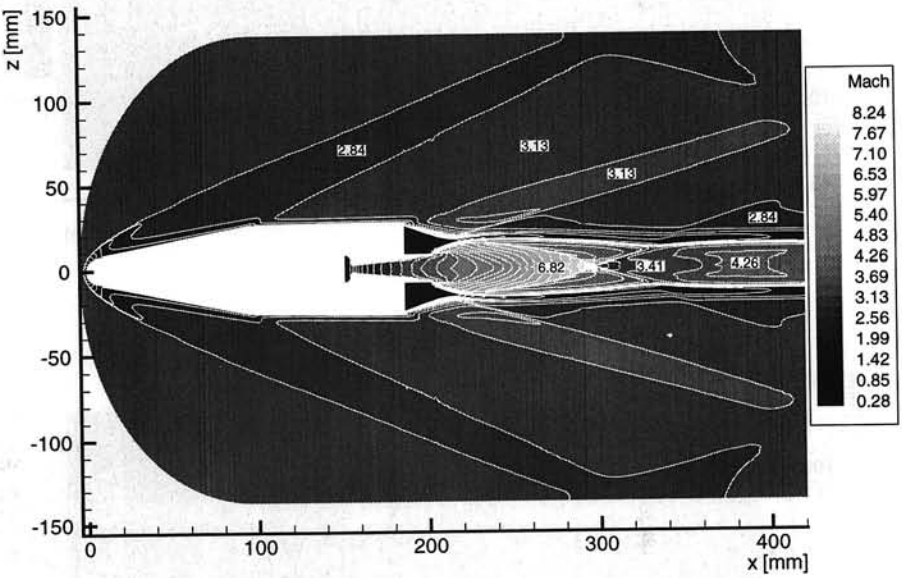

(c) Navier-Stokes, Mach-adapted Mesh

Figure 5.19: Mach Number Contour Plot, $M_\infty = 2.98$, $p_{tj}/p_\infty = 400$

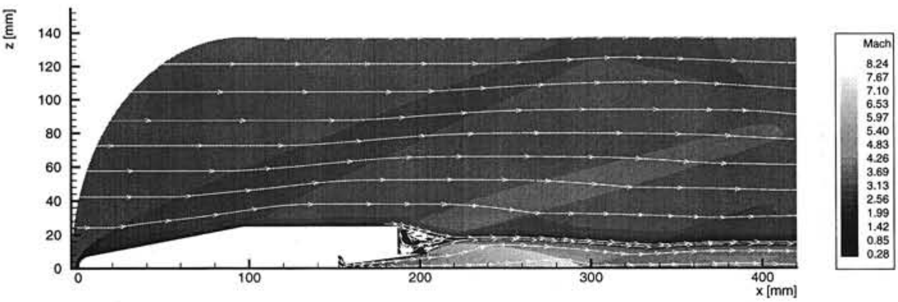

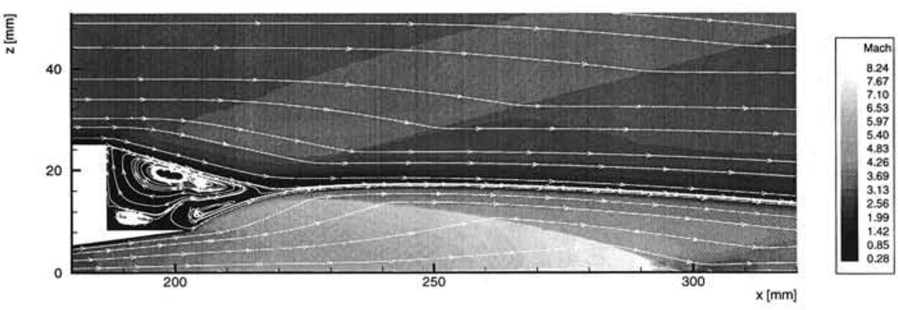

(b) Navier-Stokes Simulation, Mach-adapted Mesh, BaseJet Region

Figure 5.20: Streamlines, $M_\infty = 2.98$, $p_{tj}/p_\infty = 400$

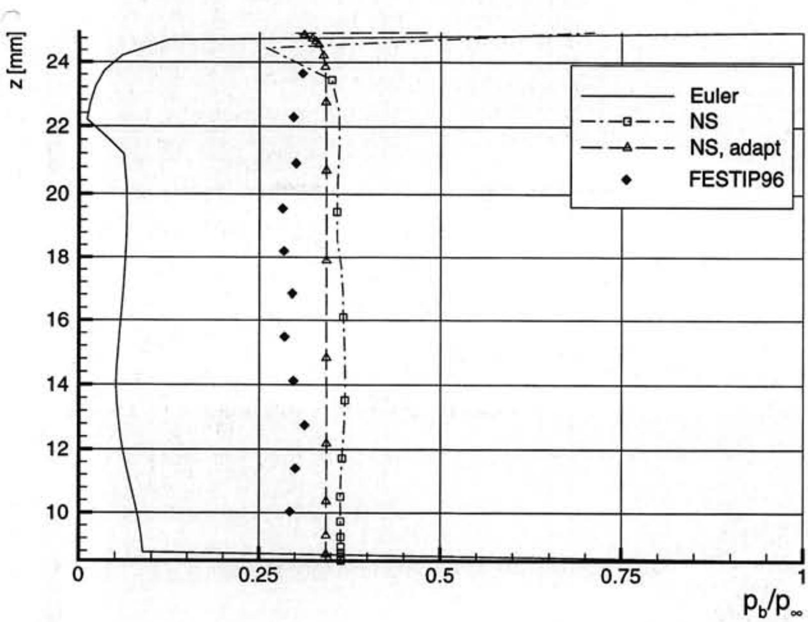

Figure 5.21: Base Pressure, $M_\infty = 2.98$, $p_{tj}/p_\infty = 400$

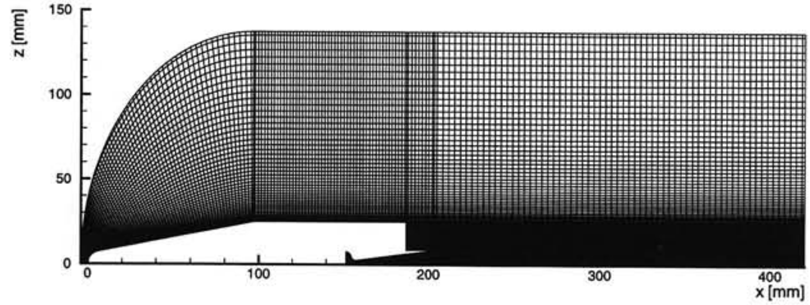

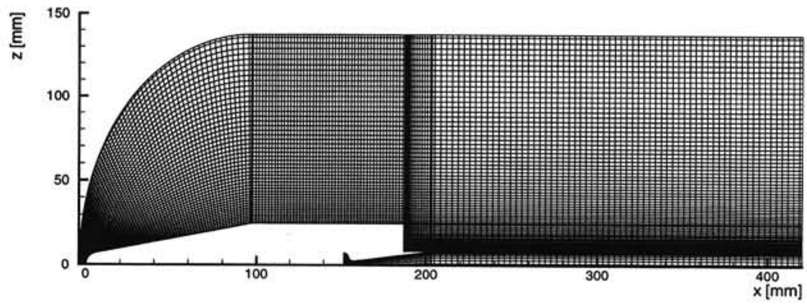

(b) Navier-Stokes Simulation

5.9 Jet-Flow, $N = p_{tj}/p_\infty = 600$

5.9.1 Mesh and Convergence

The meshes for this case are given in Fig. 5.22; no basic differences are apparent when comparing to the previous cases with jet.

As the convergence plots in Fig. 5.23, the Navier-Stokes simulation with regular mesh converges slightly faster than the Euler simulation. This can not be observed in the previous cases.

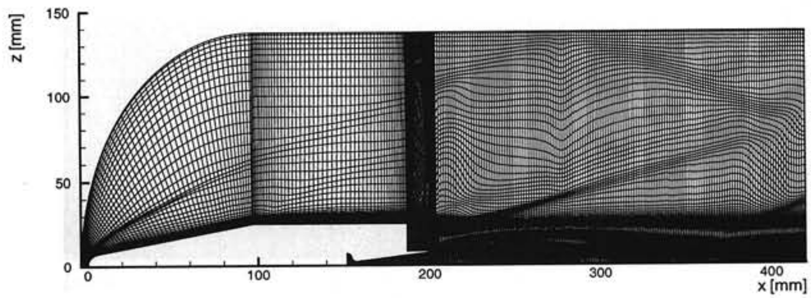

(c) Navier-Stokes, Mach-adapted Mesh

Figure 5.22: Mesh, $M_\infty = 2.98$, $p_{tj}/p_\infty = 600$

5.9.2 Mach Number Contour Plots

The Mach number plots of Fig. 5.24 show all previously mentioned features in the same quantitative way, nothing could be added in this discussion. However, a remark could be made about the area just upstream of the reflection point of the barrel shock. Because of the adaptation of the mesh the mesh points in this region can become scarce and this could cause errors in the solution.

5.9.3 Streamlines and Base Pressure

Streamline plots obtained through the numerical Navier-Stokes simulation using a Mach-adapted mesh are shown in Fig. 5.25. Again, there are two different circulation areas within the complete circulation region at the base. A relatively large circulation area, with vortices, centred in two separate areas rotating in the clockwise direction, occurs at the outer part of the base region. The second circulation area, with a vortex rotating in the counter-clockwise direction, is located at the inner part of the base region. In contrary to the previous cases, there is only one centre of vorticity in this second area. At approximately 51% of the base radius reattachment of the flow to the base seems to occur.

Base pressure distribution for this case may be found in Fig. 5.26. In the FESTIP experiments of [4] an average dimension-less base pressure of $p_b/p_\infty = 0.33$ was measured. The average value of approximately $p_b/p_\infty = 0.07$, given by the Euler computations, is too low and the base pressure is not constant. An average value of approximately $p_b/p_\infty = 0.36$ is generated by the Navier-Stokes simulation with regular mesh. For he Navier-Stokes simulation with Mach-adapted mesh the base pressure is nearly constant, but the average value of about $p_b/p_\infty = 0.36$ is again not completely in agreement with experiments, i.e., the pressures are off by some 10%. It seems that the base pressures as computed by the various techniques do not change anymore

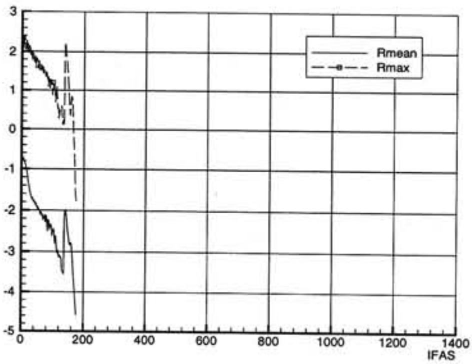

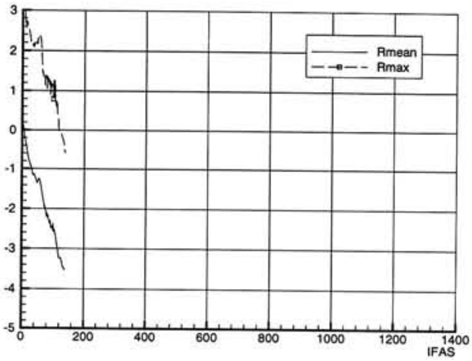

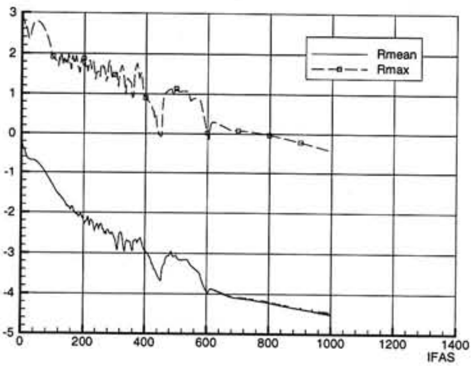

(c) Navier-Stokes, Mach-adapted Mesh

Figure 5.23: Convergence Plot, $M_\infty = 2.98$, $p_{tj}/p_\infty = 600$

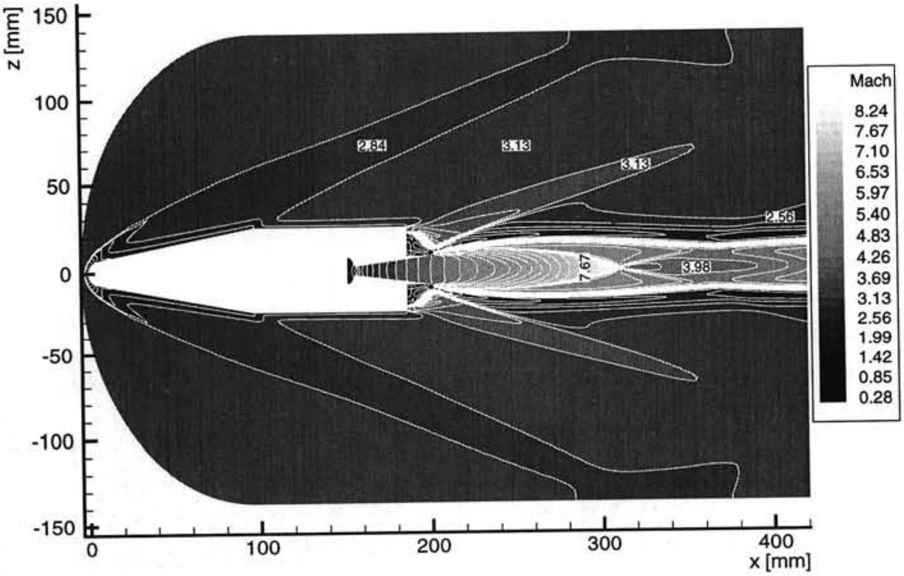

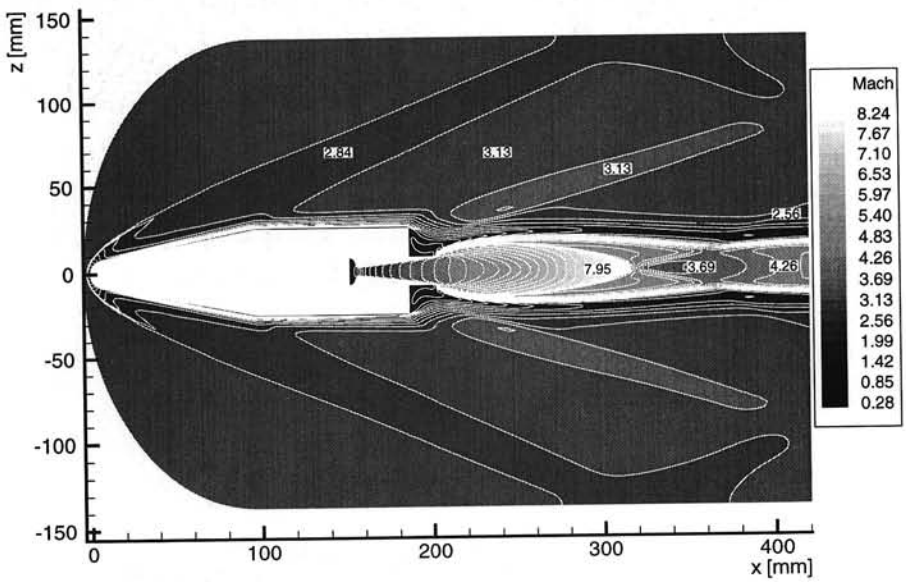

(b) Navier-Stokes Simulation

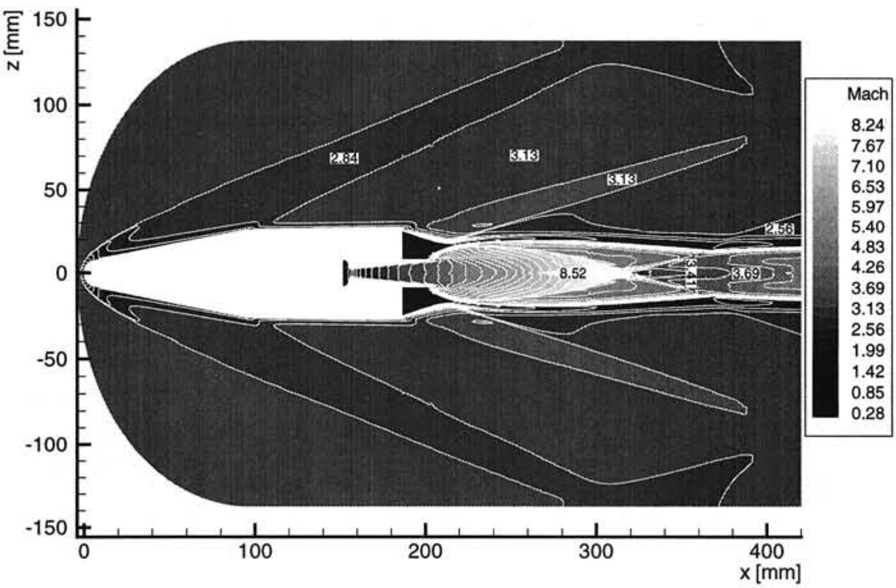

(c) Navier-Stokes, Mach-adapted Mesh

Figure 5.24: Mach Number Contour Plot, $M_{\infty} = 2.98$, $p_{tj}/p_{\infty} = 600$

p_{tj}/p_∞	p_b/p_∞, Euler	p_b/p_∞, NS	p_b/p_∞, NS adapted	p_b/p_∞, FESTIP96 exp.
no-jet	0.41	0.64	0.62	0.32
115	0.08	0.57	0.28	0.21
200	0.08	0.36	0.31	0.23
400	0.07	0.36	0.34	0.29
600	0.07	0.36	0.36	0.33

Table 5.1: Average Base Pressure, Comparison of Different Methods

with the higher values of the parameter $N = p_{tj}/p_\infty$ (compare the cases of $N = p_{tj}/p_\infty = 115$, $N = 200$, $N = 400$ and $N = 600$).

In the next section the accuracy of the calculated base pressure values will be discussed for increasing jet pressure ratio.

5.10 Comparison of Base Pressure Values

Table 5.1 shows the approximate average base pressure values of the three types of numerical simulation and the experimental data from the FESTIP investigation of [4]. Fig. 5.27 shows the graphical representation of these values. The numerical Navier-Stokes simulation with Mach-adapted mesh makes the best physical representation of the experimental base pressure distribution. Although, compared to the experimental data, the actual values are some 30% off in the cases of $N = p_{tj}/p_\infty = 115$ and $N = 200$, some 20% for $N = 400$ and some 10% for $N = 600$; the trend of the experimentally acquired static base pressure curves is followed. For higher jet pressures the base pressure prediction becomes more accurate.

The Euler simulation and the Navier-Stokes simulation with regular mesh do not give a base pressure distribution which follows the before mentioned trend. At high jet pressures the base pressure seems to be constant and independent of the parameter N. This might be caused by convergence problems in the base region, which do not occur in this manner for the simulation with Mach-adapted mesh, because it is better suited for computation of the base flow. However, no specific cause is apparent.

In all three types of simulation the case of no-jet is different from the experimental data. This might be explained by the fact that for low values of jet pressure a small difference in jet pressure causes a large difference in base pressure. An insignificant jet pressure might have occurred for the experiments because of possible leakage of the external high- pressure supply. Again, possible convergence problems might cause the discrepancy, but no particular reason is evident.

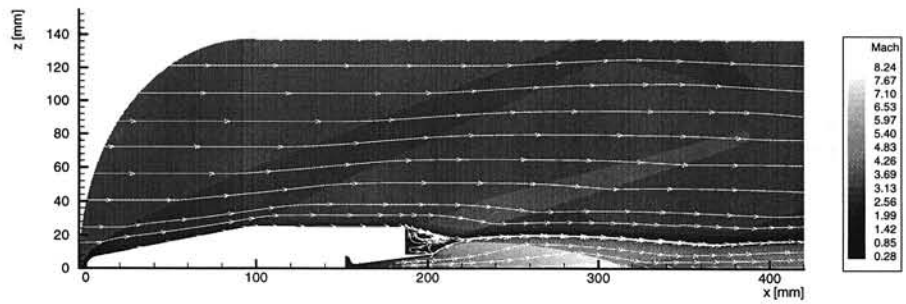

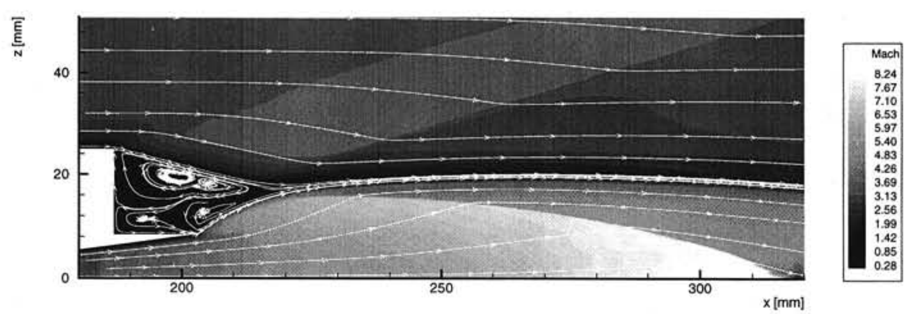

(b) Navier-Stokes Simulation, Mach-adapted Mesh, BaseJet Region

Figure 5.25: Streamlines, $M_\infty = 2.98$, $p_{tj}/p_\infty = 600$

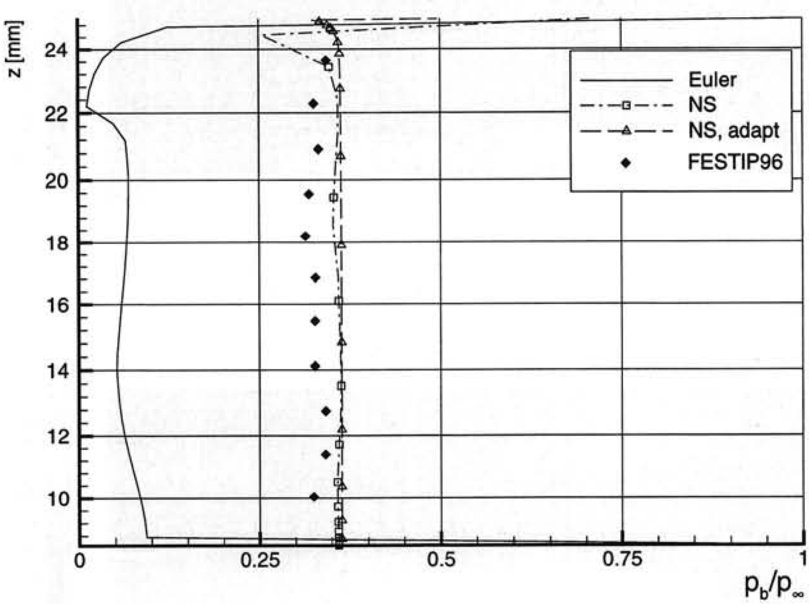

Figure 5.26: Base Pressure, $M_\infty = 2.98$, $p_{tj}/p_\infty = 600$

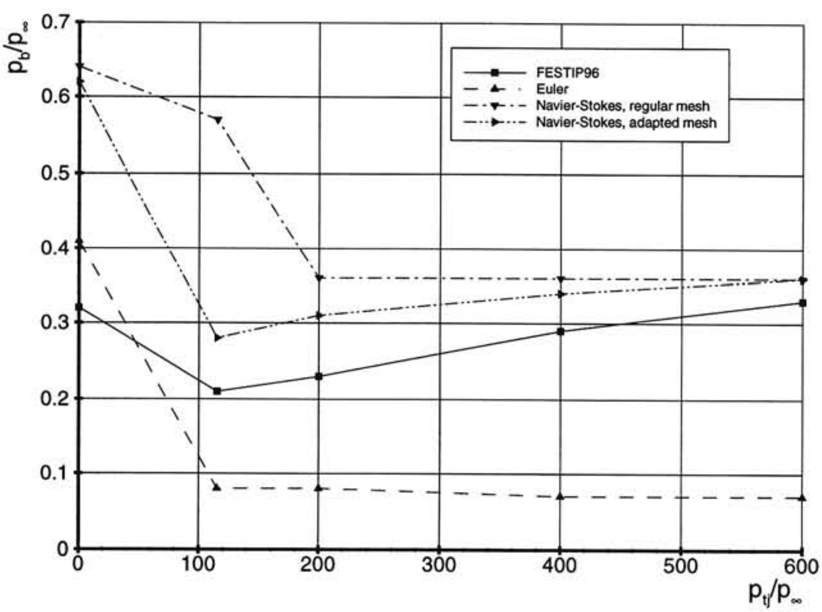

Figure 5.27: Average Base Pressure, Comparison of Different Methods

5.11 Outpluming

At first sight it looks, especially for large ratios of jet stagnation pressure to free stream pressure, as if the barrel shock and the plume shock start at a relatively small angle, concerning the amount of under-expansion. The sight of exhaust plumes at rocket launches inspires this impression. In order to be able to comment on this phenomenon, the initial expansion angle at the nozzle lip has to be known.

This expansion angle can be found by considering the flow at the lip of a nozzle with half angle δ_N, see Fig. 5.28. In the direct vicinity of the nozzle lip, a two-dimensional Prandtl-Meyer expansion is assumed. Thus, the flow at the nozzle lip turns through an angle of $\Delta\nu$ relative to the nozzle wall, depending on the ratio of the pressure before and after expansion. The overall flow expansion angle with respect to the flow axis is α, where

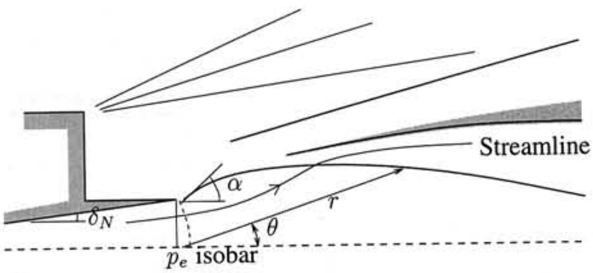

Figure 5.28: Barrel Shock and Plume Boundary

$$\alpha = \Delta\nu + \delta_N \tag{5.1}$$

The pressure at the nozzle exit, i.e., p_e, can be derived from the total jet pressure and the nozzle exit Mach number, by means of the relationship

$$\frac{p}{p_t} = (1 + \frac{\gamma - 1}{2} M^2)^{\frac{-\gamma}{\gamma-1}} \tag{5.2}$$

With a ratio of specific heats $\gamma = c_p/c_v = 1.4$ and a nozzle exit Mach number of M=4, the values of nozzle exit pressure are found as given in Table 5.2.

Assuming that the pressure after expansion is equal to the base pressure, the angle $\Delta\nu$ can be found by using the ratio of nozzle exit pressure and base pressure in combination with the equations for the Prandtl-Meyer angle. The FESTIP investigation [4] gives the experimentally obtained base pressures. The experimental data is used because of the accuracy in base pressure (see section 'Comparison of Base Pressure Values'). The base pressures and the before-mentioned ratio of pressures are shown in Table 5.2.

The initial expansion angle is found by adding the nozzle half angle of 7.5° to the calculated Prandtl-Meyer angle. The theoretical value together with the value, measured from the numerical results using a Mach-adapted mesh, of the angle α is shown in Table 5.2.

Although the measured values are not accurate and assumptions are made in calculating the theoretical values, it is clear from comparison of both these values that the observed phenomenon is normal.

p_{tj}/p_∞	p_e/p_∞	p_b/p_∞ (exp.)	p_e/p_b	α (theory)	α (measured)
115	0.76	0.21	3.61	28.2°	$\approx$ 27°
200	1.32	0.23	5.73	40.5°	$\approx$ 37°
400	2.63	0.29	9.08	53.6°	$\approx$ 49°
600	3.95	0.33	11.97	61.5°	$\approx$ 58°

Table 5.2: Initial Expansion Angle

Chapter 6

CONCLUSIONS AND RECOMMENDATIONS

Results of a single nozzle plume with a high supersonic exit Mach number of 4 exhausting in a co-flowing supersonic free stream of Mach 2.98 have been presented for a number of conditions, ranging from $p_{tj}/p_\infty = 600$ to no-jet-flow flow at Mach 2.98. Euler and Navier-Stokes simulations, for which the Reynolds numbers based on the model length were greater than $5 \cdot 10^6$, at Mach 2.98 were used to compare with experimentally obtained data [4, 14]. As may be expected Euler simulation does not provide an accurate representation of the flow field in the base region of the FESTIP-model. In order to obtain an accurate physical representation of the interaction zone mesh adaptation has been applied for a Navier-Stokes simulation.

In the present investigation the mesh adaptation seems to be responsible for increasing the number of iterations tremendously compared to the simulations with regular meshes. However, this is not comparable because both the regular meshes and the Mach-adapted meshes contained an equal amount of points. In such a case the adapted mesh provides a more accurate solution, but takes more iterations to converge because of the diminished smoothness of the mesh. Nevertheless, the Mach-adapted mesh provides a gain in accuracy, which convincingly overshadows the deterioration of the convergence.

Navier-Stokes simulations for laminar flow were made with the objective to compare various adaptations. For the numerical Navier-Stokes simulation with regular mesh the boundary layers were not accurately captured because of the fact that not enough mesh points were present in the boundary layers. The Mach-adapted mesh captures the flow features very well. However, pseudo-physical effects could be introduced when the mesh is changed in such a way that regions become devoid of mesh points or when the mesh becomes too skewed. The utilization of mesh adaptation makes it more difficult to retain sufficient smoothness, which is a disadvantage of this technique.

The simulation using the Mach-adapted mesh provides an accurate reproduction of the physical flow field, especially in the region of the interaction of the jet and the co-flowing stream.

The streamline plots obtained through the Navier-Stokes simulation with Mach-adapted mesh give some insight in the physics of the circulation region. For the case of no-jet-flow three separate regions of vorticity were found and reattachment of the flow to the model is possible. For the cases with jet-flow two separate regions of vorticity were found which were both subdivided in two and sometimes three areas of vorticity concentration. Reattachment of the flow to the base of the model could be possible at the transition from one circulation area to the other.

However, for all cases, reattachment was not accurately visualized and no sound conclusions about resulting heat-conduction can be drawn.

The Navier-Stokes simulation with Mach-adapted mesh makes the best physical representation of the base pressure distribution and the trend of the experimentally acquired static base pressure curves is followed. The Navier- Stokes simulation with regular mesh does not give a base pressure distribution which follows the before mentioned trend. The case of no-jet-flow is different from the experimental data. The no-jet-flow case is characterized by a large subsonic region, which causes convergence problems for the numerical simulations.

Finally it may be recommended to use coupled, or at least uncoupled, multi-dimensional mesh adaptation for better physical representation of the flow field. Introduction of pseudo-physical effects is a result of lack of smoothness of the mesh. Enhancement of the mesh smoothness is recommended.

REFERENCES

[1] Adamson, T.C. Jr., and Nicholls, J.A. *'On the Structure of Jets from Highly Under- expanded Nozzles into Still Air'*, Journal of the Aero/Space Sc., 1959, Vol. 26, No.1, pp 16-24.

[2] Albada, G.D. van, Leer, B. van, and Roberts, W.W. *'A Comparative Study of Computational Methods in Cosmic Gas Dynamics'*, Astron. Astrophysics, **108**:76–84, 1982.

[3] Anderson, W.K., Thomas, J.L., and Whitfield, D.L. *'Multigrid Acceleration of the Flux-split Euler Equations'*, AIAA Journal, **26**(6):649–654, 1988.

[4] Bannink, W.J., Bakker, P.G., and Houtman, E.M. *'FESTIP AEROTHERMODYNAMICS 1996: Experimental Investigation of Base Flow and Exhaust Plume Interaction'*, Memorandum M-775. Faculty of Aerospace Engineering, Delft University of Technology, March 1997.

[5] Cain, T.M. *'An Experimental Study of Under-expanded Jets'*, Report No. OUEL 1959/92, Dept. of Eng. Sc., Univ. of Oxford, 1992.

[6] Hemker, P.W. and Koren, B. *'Defect Correction and Nonlinear Multigrid for the Steady Euler Equations'*, CWI Note NM-N8801, CWI Amsterdam, 1988.

[7] Leer, B. van *'Towards the Ultimate Conservation Difference Scheme IV; A New Approach to Numerical Convection'*, Journal of Comp. Physics, **23**:276–299, 1977.

[8] Leer, B. van *'Flux-Vector Splitting for the Euler Equations'*, Lecture Notes in Physics, **170**:507–512, 1982.

[9] Moran, J.P. *'Similarity in High Altitude Jets'*, AIAA Journal, 1967, Vol. 5, No. 7, pp1343-1345.

[10] Osher, S. and Chakravarthy, S. *'Upwind Schemes and Boundary Conditions with Applications to Euler Equations in General Geometries'*, Journal of Comp. Physics, **50**:447–481, 1981.

[11] Osher, S. and Solomon, F. *"Upwind Difference Schemes for Hyperbolic Systems of Conservation Laws'*, Math. Comp., **38**:339–374, 1982.

[12] Peters, C.E., and Phares, W.J. *'The Structure of Plumes from Moderately Under-expanded Supersonic Nozzles'*, AIAA Paper 70-229, 1970.

[13] Roe, P.L. *'Approximate Riemann Solvers, Parameter Vectors and Difference Schemes'*, Journal of Comp. Physics, **43**:357–372, 1981.

[14] Schoones, M.M.J. and Bannink, W.J. *'Base Flow and Exhaust Plume Interaction, Part I: Experimental Study'*, Faculty of Aerospace Engineering, Delft University of Technology, 1998.

[15] Spekreijse, S.P. *'Multigrid Solution of the Steady Euler Equations',* PhD thesis, Delft University of Technology, 1987.

[16] Starostin, K. *'Adaptatsia vychislitelnoi setki' ('Adaptation of Computational Meshes'), Russian,* Faculty of Aerospace Engineering, Delft University of Technology, November 1996.

[17] Thompson, J.F. *'Numerical Grid Generation',* North-Holland, 1982.

[18] Venkatakrishnan, V. *'On the Accuracy of Limiters and Convergence to Steady State Solutions',* AIAA Paper 93-0880, 1993.

LIST OF TABLES

LIST OF FIGURES

Series 01: Aerodynamics

01. F. Motallebi, 'Prediction of Mean Flow Data for Adiabatic 2-D Compressible Turbulent Boundary Layers'
    1997 / VI + 90 pages / ISBN 90-407-1564-5
02. P.E. Skåre, 'Flow Measurements for an Afterbody in a Vertical Wind Tunnel'
    1997 / XIV + 98 pages / ISBN 90-407-1565-3
03. B.W. van Oudheusden, 'Investigation of Large-Amplitude 1-DOF Rotational Galloping'
    1998 / IV + 100 pages / ISBN 90-407-1566-1
04. E.M. Houtman / W.J. Bannink / B.H. Timmerman, 'Experimental and Computational Study of a Blunt Cylinder-Flare Model in High Supersonic Flow'
    1998 / VIII + 40 pages / ISBN 90-407-1567-X
05. G.J.D. Zondervan, 'A Review of Propeller Modelling Techniques Based on Euler Methods'
    1998 / IV + 84 pages / ISBN 90-407-1568-8
06. M.J. Tummers / D.M. Passchier, 'Spectral Analysis of Individual Realization LDA Data'
    1998 / VIII + 36 pages / ISBN 90-407-1569-6
07. P.J.J. Moeleker, 'Linear Temporal Stability Analysis'
    1998 / VI + 74 pages / ISBN 90-407-1570-X
08. B.W. van Oudheusden, 'Galloping Behaviour of an Aeroelastic Oscillator with Two Degrees of Freedom'
    1998 / IV + 128 pages / ISBN 90-407-1571-8
09. R. Mayer, 'Orientation on Quantitative IR-thermografy in Wall-shear Stress Measurements'
    1998 / XII + 108 pages / ISBN 90-407-1572-6
10. K.J.A. Westin / R.A.W.M. Henkes, 'Prediction of Bypass Transition with Differential Reynolds Stress Models'
    1998 / VI + 78 pages / ISBN 90-407-1573-4
11. J.L.M. Nijholt, 'Design of a Michelson Interferometer for Quantitative Refraction Index Profile Measurements'
    1998 / 60 pages / ISBN 90-407-1574-2
12. R.A.W.M. Henkes / J.L. van Ingen, 'Overview of Stability and Transition in External Aerodynamics'
    1998 / IV + 48 pages / ISBN 90-407-1575-0
13. R.A.W.M. Henkes, 'Overview of Turbulence Models for External Aerodynamics'
    1998 / IV + 40 pages / ISBN 90-407-1576-9
14. G. Schouten, 'The Two-Dimensional Soundfield of a Vortex Moving Around the Sharp Edge of a Half-Plane'
    1998 / VI + 26 pages / ISBN 90-407-1730-3
15. M.M.J. Schoones / W.J. Bannink, 'Base Flow and Exhaust Plume Interaction. Part 1: Experimental Study'
    1998 / VIII + 64 pages / ISBN 90-407-1747-8

16. M.M.J. Schoones / W.J. Bannink, 'Base Flow and Exhaust Plume Interaction. Part 2: Computational Study'
1998 / VIII + 86 pages / ISBN 90-407-1748-6

Series 02: Flight Mechanics

01. E. Obert, 'A Method for the Determination of the Effect of Propeller Slipstream on a Static Longitudinal Stability and Control of Multi-engined Aircraft'
1997 / IV + 276 pages / ISBN 90-407-1577-7
02. C. Bill / F. van Dalen / A. Rothwell, 'Aircraft Design and Analysis System (ADAS)'
1997 / X + 222 pages / ISBN 90-407-1578-5
03. E. Torenbeek, 'Optimum Cruise Performance of Subsonic Transport Aircraft'
1998 / X + 66 pages / ISBN 90-407-1579-3

Series 03: Control and Simulation

01. J.C. Gibson, 'The Definition, Understanding and Design of Aircraft Handling Qualities'
1997 / X + 162 pages / ISBN 90-407-1580-7
02. E.A. Lomonova, 'A System Look at Electromechanical Actuation for Primary Flight Control'
1997 / XIV + 110 pages / ISBN 90-407-1581-5
03. C.A.A.M. van der Linden, 'DASMAT-Delft University Aircraft Simulation Model and Analysis Tool. A Matlab/Simulink Environment for Flight Dynamics and Control Analysis'
1998 / XII + 220 pages / ISBN 90-407-1582-3
04. S.K. Advani, 'The Kinematic Design of Flight Simulator Motion-Bases'
1998 / XVIII + 244 pages / ISBN 90-407-1671-4
05. J.M. Maciejowski, 'Predictive Control. A Lecture Course Given in the Aerospace Engineering Faculty TU Delft'
1998 / XII + 156 pages / ISBN 90-407-1714-1

Series 05: Aerospace Structures and Computional Mechanics

01. A.J. van Eekelen, 'Review and Selection of Methods for Structural Reliability Analysis'
    1997 / XIV + 50 pages / ISBN 90-407-1583-1
02. M.E. Heerschap, 'User's Manual for the Computer Program Cufus. Quick Design Procedure for a CUt-out in a FUSelage version 1.0'
    1997 / VIII + 144 pages / ISBN 90-407-1584-X
03. C. Wohlever, 'A Preliminary Evaluation of the B2000 Nonlinear Shell Element Q8N.SM'
    1998 / IV + 44 pages / ISBN 90-407-1585-8
04. L. Gunawan, 'Imperfections Measurements of a Perfect Shell with Specially Designed Equipment (UNIVIMP)
    1998 / VIII + 52 pages / ISBN 90-407-1586-6

Series 07: Aerospace Materials

01. A. Vašek / J. Schijve, 'Residual Strenght of Cracked 7075 T6 Al-alloy Sheets under High Loading Rates'
    1997 / VI + 70 pages / ISBN 90-407-1587-4
02. I. Kunes, 'FEM Modelling of Elastoplastic Stress and Strain Field in Centre-cracked Plate'
    1997 / IV + 32 pages / ISBN 90-407-1588-2
03. K. Verolme, 'The Initial Buckling Behavior of Flat and Curved Fiber Metal Laminate Panels'
    1998 / VIII + 60 pages / ISBN 90-407-1589-0
04. P.W.C. Provó Kluit, 'A New Method of Impregnating PEI Sheets for the *In-Situ* Foaming of Sandwiches'
    1998 / IV + 28 pages / ISBN 90-407-1590-4
05. A. Vlot / T. Soerjanto / I. Yeri / J.A. Schelling, 'Residual Thermal Stresses around Bonded Fibre Metal Laminate Repair Patches on an Aircraft Fuselage'
    1998 / IV + 24 pages / ISBN 90-407-1591-2
06. A. Vlot, 'High Strain Rate Tests on Fibre Metal Laminates'
    1998 / IV + 44 pages / ISBN 90-407-1592-0
07. S. Fawaz, 'Application of the Virtual Crack Closure Technique to Calculate Stress Intensity Factors for Through Cracks with an Oblique Elliptical Crack Front'
    1998 / VIII + 56 pages / ISBN 90-407-1593-9
08. J. Schijve, 'Fatigue Specimens for Sheet and Plate Material'
    1998 / VI + 18 pages / ISBN 90-407-1594-7
09. J. Schijve, 'The Significance of Fractography for Investigations of Fatigue Crack Growth under Variable-Amplitude Loading'
    1998 / IV + 34 pages / ISBN 90-407-1716-8

10. M.J.L. van Tooren / Z.C. Roza, 'Finite Difference Methods for Stress Analysis of Adhesive Bonded Joints. The Design of a MATLAB Adhesive Toolbox'
1998 / VIII + 94 pages / ISBN 90-407-1717-6

Series 08: Astrodynamics and Satellite Systems

01. E. Mooij, 'The Motion of a Vehicle in a Planetary Atmosphere'
1997 / XVI + 156 pages / ISBN 90-407-1595-5
02. G.A. Bartels, 'GPS-Antenna Phase Center Measurements Performed in an Anechoic Chamber'
1997 / X + 70 pages / ISBN 90-407-1596-3
03. E. Mooij, 'Linear Quadratic Regulator Design for an Unpowered, Winged Re-entry Vehicle'
1998 / X + 154 pages / ISBN 90-407-1597-1

A computational study of the flow field along an axi-symmetric body with a single operating exhaust nozzle has been performed in the scope of an investigation on base flow-jet plume interactions. Results of a single nozzle plume with a high supersonic exit Mach number of 4 exhausting in co-flowing supersonic free stream of Mach 2.98 are presented for a number of jet stagnation pressure to free stream static pressure ratios, ranging from P_{tj}/P_{∞} = 600 to no-jet flow at Mach 2.98. These conditions were used to validate the numerical Euler and Navier-Stokes simulations with experimentally obtained data [4, 14].

Euler and Navier-Stokes simulations have been made in combination with regular meshes. In order to obtain a better physical representation of the interaction zone mesh adaptation has been applied for a Navier-Stokes simulation. One-dimensional adaptation to the Mach number distribution has been applied along fixed lines in the radial direction. In this way the flow field could be accurately portrayed.

The three numerical simulation techniques are compared using flooded Mach-number contour plots. The Navier-Stokes simulation with Mach-adapted mesh provided the basis for comparison with experimental results. A physical description of the flow field in the base region, or cavity, is presented using streamlines. Reattachment of the flow to the base of the model, which results in heat-transfer to the surface, has been found to be possible at approximately 45% to 50% of the base radius, measured from the centerline. However, reattachment has not been accurately visualized. Base pressure distributions obtained through all three different types of numerical simulation are presented in order to compare to the experimental data. No proper reproduction of the experimental P_b/P_{∞} - P_{tj}/P_{∞}curve (see [4, 14] could be attained.

ISBN 904071748-6

9 789040 717482

DELFT AEROSPACE
ENGINEERING & TECHNOLOGY